ETH
Eidgenössische Technische Hochschule Zürich
Swiss Federal Institute of Technology Zurich

MASTER THESIS

Characterization of Coplanar Waveguide Resonators in Parallel Magnetic Fields

Author:
Florian LÜTHI

Supervisor:
Dr. Milan ALLAN

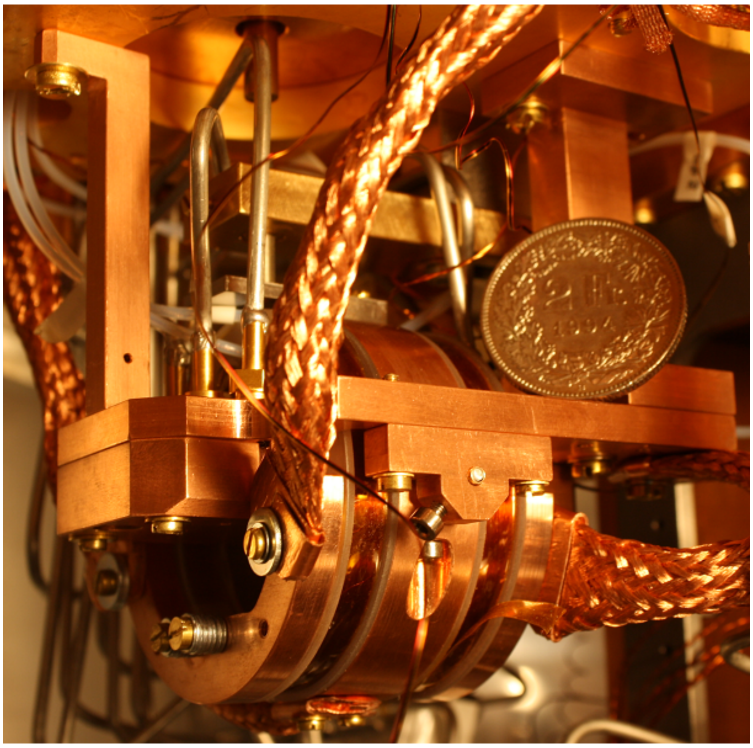

June 20, 2014

Abstract

Magnetic fields lift the spin degeneracy in an electron. For fields on the order of hundreds of Millitesla, the transition frequency between the two spin states lies in the Gigahertz regime. Therefore, superconducting circuits that operate at these frequencies can be used to probe this splitting. A possible application is an electron spin resonance imaging technique, comparable to nuclear magnetic resonance. But before this can be realized, an understanding of the behavior of superconducting coplanar waveguide resonators in magnetic fields is required. This thesis aims to get a quantitative understanding of the dissipation and its hysteretic behavior that arises due to Abrikosov vortices. A sample holder that enables tilting of magnetic field is designed. Measurements of the losses in the resonator depending on various parameters are performed. An analytical model that enables the quantitative description of the measured field dependent losses in the resonator is developed.

Contents

List of Figures

1 Motivation

A superconducting coplanar waveguide is basically a two dimensional coaxial cable. The signal travels on a superconducting center conductor. Gaps without superconducting material insulate it from the two superconducting ground planes. If the center conductor is interrupted at two positions that act as capacitances, the intermediate part will serve as a resonator. Its resonance frequency is determined by its length and material properties. The goal of this thesis is to study such coplanar waveguide resonators in strong magnetic fields applied parallel to the plane. We will get an understanding for hysteresis effects that appear in the resonator if the magnetic field is changed in direction. Also, we will see the effects of tilting the magnetic field on the properties of the resonator. But let's first see why this is an interesting subject to study.

Nuclear magnetic resonance has proven to be a very useful imaging technique with a wide range of applications. A NMR apparatus applies a strong, static magnetic field $\boldsymbol{B}_0$. This magnetic field lifts the degeneracy of the energy levels of the spin in a nucleus. This results in an energy difference $E_{mag} = -\boldsymbol{\mu} \cdot \boldsymbol{B}_0$ between these levels, where $\boldsymbol{\mu}$ is the spin magnetic moment. The corresponding frequency of to this energy difference is given as $f_{Res} \equiv \frac{\omega_L}{2\pi} = \frac{\boldsymbol{\mu B}}{h}$, where h is Plank's constant. If $\boldsymbol{\mu}$ is parallel to a field of strength 1 T, the resonance frequency is 42.5 MHz.

As it is the energetically favorable direction, the magnetic moments of the protons will align parallel to the applied magnetic field. Now, an additional (weak) magnetic ac field is applied with a coil perpendicular to the strong magnetic field (Purcell setup). The protons will start to Larmor precess, as the torque $\boldsymbol{\Gamma} = \boldsymbol{\mu} \wedge \boldsymbol{B}$ acts on them. But this again induces an ac voltage in the coil which is opposed to the one applied. Therefore, the sender needs more power. If the sender is weak, this leads to a detectable reduction in the amplitude.

Now one can imagine doing this for electrons as well. The magnetic moment of electrons is the Bohr magneton, $\mu_B = 9.27 \cdot 10^{-24}$ J/T, which leads to a resonance frequency of 28 GHz in a field of 1 T. This frequency range can be addressed using superconducting circuits and microwave electronics. A sample of organic molecules with electrons that behave almost like free electrons is placed on top of the center conductor of a superconducting coplanar waveguide resonator, as schematically depicted in Figure 1. The radio frequency current in the resonator yields a time varying magnetic field the electrons interact with. Like this, the resonance frequency of the electrons in the sample can be probed. To get spatial resolution, the static field needs to be spatially varying. This makes the frequencies of the free electron spins vary in space

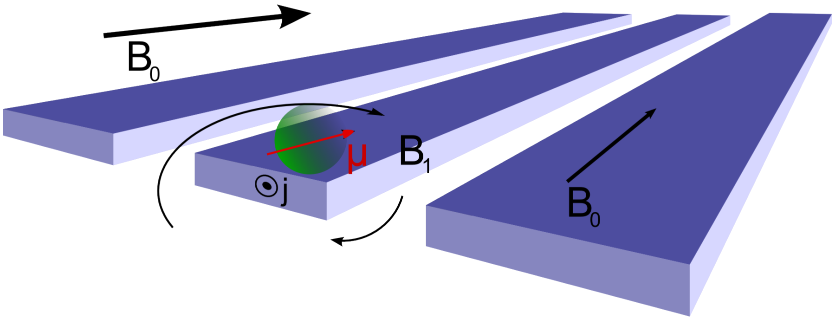

Figure 1: The three solid boxes indicate a coplanar waveguide resonator. A strong magnetic field $\boldsymbol{B}_0$ is applied in parallel. This orients the spin magnetic moment $\boldsymbol{\mu}$ of the free electrons of a sample lying on the center conductor. A current $\boldsymbol{j}$ in the center conductor of the coplanar waveguide resonator yields a perpendicular *ac* magnetic field $\boldsymbol{B}_1$.

as well, and therefore one could detect them space resolved.

But in order to use this technique, it is important to know the behavior of superconducting resonators in strong parallel magnetic fields. The challenge is to control resonators in a way that they still have high quality factors and are as magnetic field independent as possible. Also, it would be useful to have a theoretical description of how these losses come about. During this thesis, a sample holder is built which that enables the above described measurement. It is then used to characterize the losses of resonators due to a strong parallel magnetic field.

2 Requirements for the Sample Holder

Field Strength and Frequency In this section we shall look at what the sample holder needs to perform to carry out the experiment described above. From this we will deduce its requirements. In order to see a splitting of an electron spin, one needs an external magnetic field. The strength of the magnetic field needed can be calculated from the energy difference ΔE of the two energy levels of a free electron in a magnetic field,

$$\Delta E = 2\boldsymbol{\mu} \cdot \boldsymbol{B},$$

where $\boldsymbol{\mu}$ is the magnetic moment of the electron and $\boldsymbol{B}$ is the applied magnetic field. We can express $\boldsymbol{\mu}$ as $\mu_B \cdot \hat{\mu}$ where μ_B is the Bohr magneton and $\hat{\mu}$ is the unit vector pointing in direction of the magnetic moment of the electron. As we need to be able to detect the transition frequency, we can equate this with the photon energy,

$$E = hf,$$

with f being the frequency of the photon and h the Planck constant. Note, that f denotes the frequency in Hertz, and not the angular frequency ω in rad/s. This gives us a frequency of, assuming collinearity of $\boldsymbol{\mu}$ and $\boldsymbol{B}$,

$$f = \frac{2\mu_B B}{h} = 28 \cdot B \, \frac{\mathrm{GHz}}{\mathrm{T}}. \tag{1}$$

Now there is a trade off for the frequency that should be used. As it gets increasingly difficult to make stronger magnetic fields on the one hand side and the microwave electronics of the Quantum Device Lab is construed for frequencies in the Gigahertz regime. The decision to aim for a magnetic field of magnitude $0.3\,\mathrm{T}$ was made. This yields frequency of $f = 8.4\,\mathrm{GHz}$.

Additional Properties of the Field The magnetic field should be as homogeneous as possible over the whole sample. This requires the coils used to be in a Helmholtz like configuration. These two requirements are somewhat difficult to satisfy at the same time, because it requires large coils in comparison to the sample. But this in turn is not favorable, as then there need to be more windings or a stronger current which is again harder to integrate. This leads to a trade off for the coil size and placement.

Also, the field should be as parallel as possible to the sample, such that there is the least possible magnetic field perpendicular to the sample. As each sample is glued in a slightly different way into the PCB, one can not assume that a field that is parallel to some plane given by the sample holder will be parallel to the chip. Therefore it is required that the field is tiltable. Note that it is not realistic to make a tiltable sample, as this would require moving radio frequency cables which is not practicable. Therefore, a system that allows tilting of the coils is required. But then again, this system needs to suppress vibrations that could occur due to the presence of movable parts.

Setup Compatibility In order to increase the efficiency of a measurement procedure, an idea in the Quantum Device Lab is that as many parts as possible should be standardized. This includes not only the microwave electronics and the software used, but also the placement of the connectors on the PCBs. Standardization has the advantage that only one kind of PCBs is required, which facilitates several processes. But in the present case it also gives restrictions on the placement of the coils, as the connectors themselves have a certain height and need to be addressed with rather rigid cables.

Thermalization A rapid cool down needs to be ensured. This can be achieved by having only little thermal mass with a good themalization. If large surfaces touch the cold stage a good thermalization can be realized. An important issue is the radio frequency and dc cabling, as these cables are connected to warmer stages and therefore yield a considerable thermal load. The thermal transport $\dot{Q}$ can be estimated with the formula (3.32) from [1]

$$\dot{Q} = \frac{A}{L} \int_{T_1}^{T_2} \kappa(T) \mathrm{d}T, \tag{2}$$

where L denotes the cable length, A its cross section and $\kappa(T)$ the temperature dependent thermal conductivity coefficient. In order to reduce the thermal load it is therefore advisable to use as few as possible as thin as possible cables. If the thermal load is high, the temperature of the cold stage will rise, as the cooling power of the pulse tube is temperature dependent.

Other Considerations It is important that an easy access to the sample is provided, such that not the whole sample holder needs to be disassembled in order to change the sample. This not only saves a lot of time but also protects from defects due to handling the parts.

Another issue is the shielding of the magnetic field towards the outside.There are sensitive measurements going on in the vicinity of the setup. It is therefore good practice to reduce the magnetic field emitted from the coils by putting a passive shield of high magnetic permeability around the coils. The material for this should preferably be Cryoperm, as it also shows good magnetic properties even at low temperatures [2,3].

The sample holder will be placed in an already existing pulse tube cooled cryostat, the Arctic (trAnsport, Rf and optiCal tThree kelvIn Cryostat) [4]. It is essentially self-designed by Gabriel Puebla-Hellmann. As there is already an existing sample holder in the Arctic, compatibility with it needs to be ensured.

3 Realization of a Compact Sample Holder

3.1 Design of the Coils

Field Characterization In order to reduce the thermal load of the dc wiring for the coils, very thin wire is used, see Equation 2. Like this, more windings allow for a lower current. The wire used has a diameter (insulated) of 36 μm. The superconducting filament has a diameter of 15 μm [5]. We thought that we optimized the design for a current of 0.3 A. But due to a

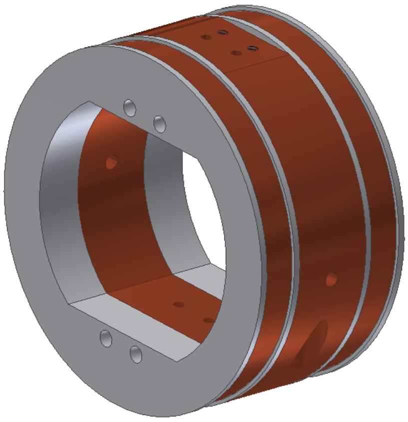

Figure 2: The coils made of a Stycast body (white) with superconducting wire. Between the coils is a copper part for thermalization.

foolish and embarrassing mistake by the author that was found only after completion of the coils, the actual achievable field is only 0.13 T. (The simulations for the field were performed in Mathematica. There, the symbol I was used to denote the current of 0.3 A. But this symbol denotes the imaginary unit in Mathematica, therefore the estimations for the field strength were off by a factor three.) The design for the coils was made in Autodesk Inventor, a CAD program, and is is displayed in Figure 2. The formulas for the field of a coil of finite length were taken from [6, 7]. The plots characterizing the coil field are shown in Figure 3 where the magnitude of the field in the surrounding of the coils is plotted. The lines in Figure 3a show regions of the same field strength. The z-direction lies in the coil axis, ρ is the radial component.At the edge of the plot some numerical errors can be seen.

A more detailed characterization of the field close to the sample can be obtained by slicing it in z-direction, as shown in Figure 3b. There, a close up of the field in axial direction is shown. The thick black lines mark the region inside which the sample will be placed. The homogeneity H of the field over the sample region is defined here by taking the ratio between the field strength on the edge of the region and at the origin. This yields

$$H = \frac{B(z = 3.5\,\mathrm{mm})}{B(0)} = \frac{0.128\,\mathrm{T}}{0.129\,\mathrm{T}} = 0.99. \tag{3}$$

Thermalization It is important that the coils are thermalized well. This can not be achieved by just thermalizing the ends of the wires to the cold stage, as the thermal transport through a thin wire is poor, compare Equation 2. A better thermalization can be achieved by pressing the coil bodies

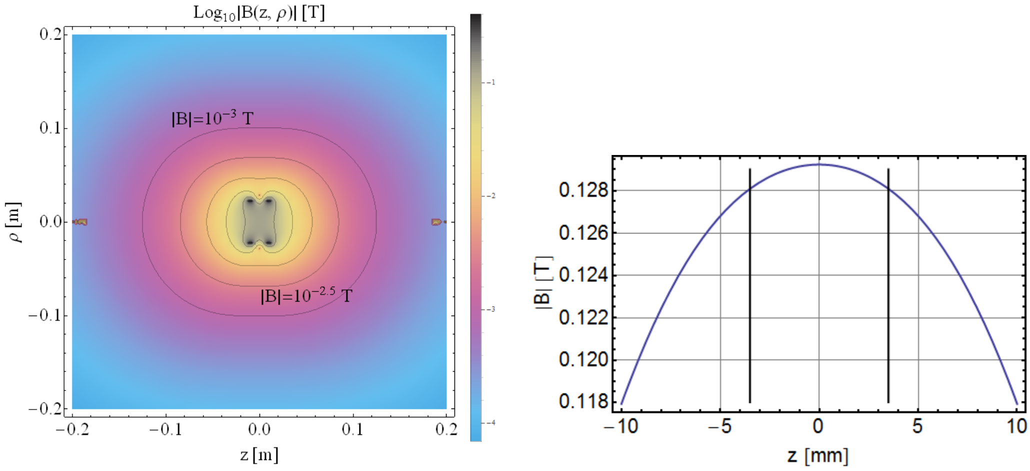

(a) Magnitude of the field sourced by the coils.

(b) Magnitude of the field on the z-axis.

Figure 3: The magnitude of the magnetic field sourced by the coils. The lines in Figure (a) show regions of the same field strength. The solid black lines in (b) indicate the sample region.

against an intermediary copper part. This makes the contact surface much larger. Also, this copper parts allows the mounting of copper braids for better thermalization with the cold stage.

We decided to make the coil bodies out of Stycast 1266. This is a two component epoxy that has a good thermal conductivity coefficient $\kappa(T)$ [1] for a plastic even at low temperatures. We decided not to use copper - which would have a much better thermal conductivity - because we feared that any edges could cut the fragile wire. The Stycast parts were made by ourselves. The receipt for this is presented in appendix A. The coil bodies were the machined in the workshop of the physics department, see Figure 4a. The winding of the coils was performed extern in a company called Werap, for which we also provided a winding tool. As the forces acting on the coil body from the winding are quite big, one of the coil bodies cracked as the technician at Werap took it out of the winding tool, see Figure 4b. This probably hampered the thermalization, as the contact surface is not as big any more.

Later on during the improvement iterations for the coils, several additional thermalization elements were used. First, more copper braids with enhanced quality were mounted. The quality of the copper braids can be increased by using excessive violence to crimp together the braid and the copper sheet. We did this using a bench vice. Also, it was tried to increase

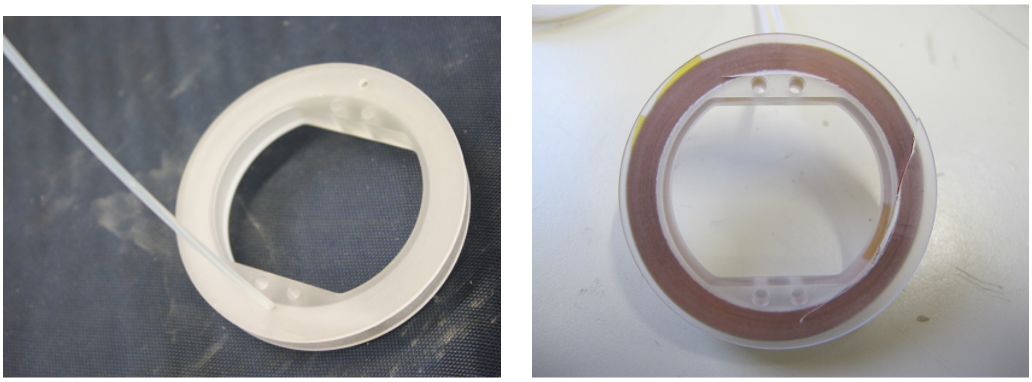
(a) A Stycast coil body with a teflon tube to protect the wire sticking out.

(b) The coil that had a crack in the coil body after the winding procedure.

Figure 4: The coils, before the winding and after. The second coil did not suffer any damage.

the pressure of the screws on the coil bodies. This is assumed to be a problem, as the Stycast coil bodies contract stronger than the brass screws. This can be compensated by using stainless steel spacers or washers. Brass has a relatively high thermal contraction, whereas stainless steel has not, [1]. Cooling down then leads to an effective tightening of the screws if there is sufficient stainless steel. This can be calculated easily. As a third measure, further copper elements were produced and pressed against the outer surface of the coil bodies. These copper parts can again be thermalized with copper braids.

Current Source The power source needs to be able to source a current of at least 0.3 A in bot h directions. Also, it would be useful if it would source current and not voltage, as the current goes directly into the formula for the magnetic field. This enables a better control of the field. Out of these reasons a Keithley 2450 was bought, which is a source measure unit. It can source current and voltage, and also measure current and voltage during it sources. This has proven to be useful during the investigation of the quenches. Like this, the current could be steadily increased, and the voltage measured at the same time. Like this, the dissipated power can be observed and some conclusion can be drawn on the behavior of the coils.

The Keithley 2450 is controlled via LAN using SCPI commands in a LabView interface. Something that needs to be taken care of is the setting of the voltage limit when sourcing a current. If the range is set on automatic, the output is first turned off, then the limit is changed and only then the desired current is sourced. This problem can be circumvented by setting the maximum limits before sweeping the current.

In order to protect both the coil and the current source from damages due to induction, one could in principal use a shunt resistor. Here, this is solved in a bit more elaborated way. First, we will estimate the voltage that could arise due to a power outage (which is apparently not that uncommon in this building). The induction voltage U is given as

$$U = L \cdot \frac{\mathrm{d}i}{\mathrm{d}t} \approx L \cdot \frac{\Delta i}{\Delta t}, \tag{4}$$

where i denotes the current, t the time and L the inductance. The inductance can be derived by equating Faraday's law

$$U = -N\frac{\Delta\Phi}{\Delta t} = -NA\frac{\Delta B}{\Delta t} \tag{5}$$

where Φ is the magnetic flux and A is the area with equation 4. For this, express $B = b \cdot i$ where b is the current to field conversion factor for the maximum field. Like this, we obtain

$$L = NA \cdot b \approx 20'000 \cdot (2.3 \cdot 10^{-2})^2\pi \cdot 0.5 \approx 17\,\mathrm{H} \tag{6}$$

per coil. Therefore, using Equation 4 we get an induced voltage of

$$U = L \cdot \frac{\Delta i}{\Delta t} \approx 2 \cdot 17 \cdot \frac{0.3}{0.01} \approx 1\,\mathrm{kV} \tag{7}$$

if the maximal current is sourced and drops during half an oscillation period of the power grid ac current.

To prevent damage from such potential peaks, varistors can be used. These are non linear circuit elements that are not conducting under a certain threshold voltage, but conducting above it. Also it makes sense to put a low pass filter between the power source and the coils to damp high-frequency oscillations. Both of these things are implemented separately for each port. This is combined in the circuit shown in Figure 5. The resistors have a value of $80\,\Omega$. Retrospectively, one could also have taken a lower value. The capacitors have $22\,\mu\mathrm{F}$ which is limited by the immediate availability of stronger non-polarized capacitors. This yields a cutoff frequency of

$$f_0 = \frac{1}{2\pi RC} \approx 90\,\mathrm{Hz}.$$

Due to the large value of the resistors, a power of $P = R \cdot I^2 \approx 15\,\mathrm{W}$ is dissipated when $0.3\,\mathrm{A}$ are sourced. So far, this did not yield problems with the cooling of the box.

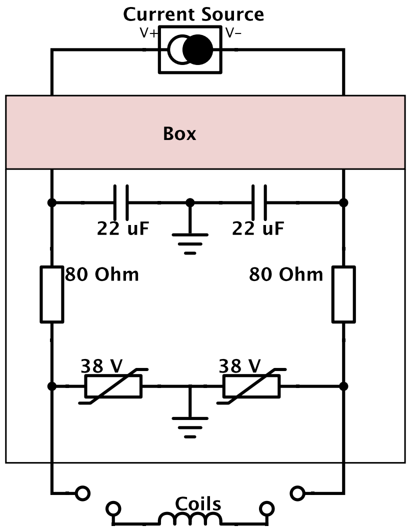

Figure 5: The circuit implemented to protect the coils and the current source from induction voltages. There are two low pass filters and two varistors.

Shield In order to shield other measurement setups from the magnetic field we generate it is easiest if a shield is put around our setup. We decided to make a passive shield out of Cryoperm [2, 3] that has good magnetic properties even at low temperatures. It was fabricated, but not yet annealed. Annealing the shield would be necessary as this greatly enhances the properties of the shield. Also, it was not tested so far.

3.2 DC Wiring

It is necessary to pull at least two dc wires into the fridge. Usually, these wires yield a big heat load, as they need to be made of a material that is electrically well conducting. As electrical $\sigma(T)$ and thermal conductivity $\kappa(T)$ are linked by the Wiedemann-Franz-Law,

$$\frac{\kappa(T)}{\sigma(T)} = L \cdot T$$

where T is the temperature and $L \approx 2.4 \cdot 10^{-8}\,\mathrm{W\Omega K^{-2}}$ is the Lorenz number, the thermal conductivity of such a wire is high as well. Therefore, the thermal transport given by Equation 2 is high.

But in order to get the total thermal load, one needs also to account for the electrical resistance R of the wire that will lead to heating, with

$P = R \cdot I^2$. As the total resistance is given as

$$R = \rho \frac{l}{A} \tag{8}$$

there is an optimal wire radius r at a given wire length. If the calculation is done in more extent, one has to consider the heating of the thermalization wire of length l' as well, and not only the wire length l that connects the two plates. Using Equations 2 and 8 the total heat load is then approximately given as

$$P = \rho(3\,\mathrm{K}) \frac{l'}{\pi r^2} + \tilde{\rho} \frac{l}{\pi r^2} + \frac{A}{l} \tilde{\kappa} \left(T_2^2 - T_1^2 \right), \tag{9}$$

where $\tilde{\rho}$ and $\tilde{\kappa}$ are temperature averaged values. The challenge now is of course to get a good estimate for these values, which is not entirely easy. This is because these values strongly depend on the degree of purity of the material. In our case we expect for a wire diameter of 0.3 mm and lengths $l \approx l' \approx 0.6\,\mathrm{m}$ a heat load of 3 mW if we use $\tilde{\rho} \approx 5 \cdot 10^{-10}\,\Omega\mathrm{m}$ and $\tilde{\kappa} \approx 10\,\mathrm{W/Km}$. All these values are to be taken with care, as it is hard to determine them precisely.

3.3 Mechanics

It was clear rather quickly that a flexure bearing will be the way of choice, as it reduces the number of moving parts. Also, no freezing problems will occur and no lubrication is necessary. This facilitates the construction and usage. The problem with flexure bearings is that vibrations can occur. These need to be suppressed as good as possible such that the measurement wont be distorted. We decided to use a torsional spring in the axis of rotation of the coils. This design has the lowest spring constant in torsional direction, hence vibrations in up-down and back-forward direction are suppressed. As a material for the springs we choose Beryllium Copper (Cu 98 Be 2) as it has good spring characteristics even at low temperatures. The drawback is the danger of inhaling its toxic dust upon machining it. The torsion (shear) modulus of BeCu is $G = 0.53 \cdot 10^6$ bar, the Young modulus is $E = 1.3 \cdot 10^6$ bar. To determine the required geometry of the spring, following calculations were performed. The torque τ is given as

$$\tau = -\kappa\theta = dF \tag{10}$$

where κ is the torsional spring constant, θ the deflection angle, and F is the force required to produce a torque τ when it acts a distance d away from the rotation axis, see Figure 6. The force is exerted from a micrometer screw that presses on the coils. The micrometer screw is driven by a stepper motor (Nanotec, ST4209M1206) that can make steps of 0.9°. Like this we get a high resolution in the torsion angle of the coils. The torsion angle can be expressed as [9,10]

$$\theta = \frac{\tau L}{G I_T} \tag{11}$$

where L is the beam length, G the shear modulus and I_T is the torsional moment of inertia which is the same as the polar moment of inertia for circular cross sections. If the inner radius of the tube is r and the outer is R, then

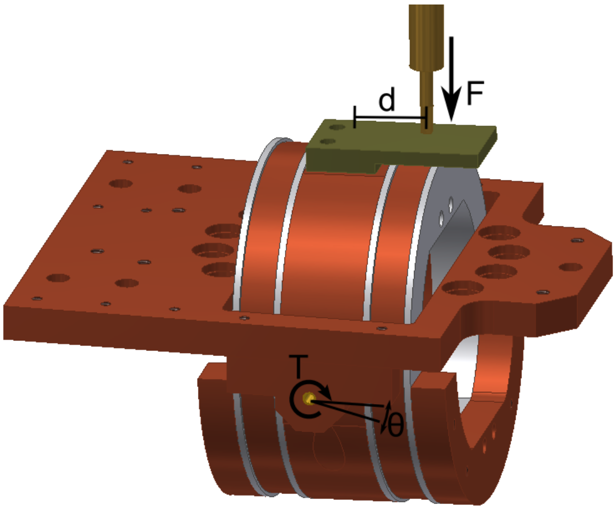

Figure 6: The schematic of how the coils tilt. The rotation axis are the BeCu tubes (golden) on which a torque τ acts due to a force F at a distance d away acting on the coils.

$$I_T = \int_A r^2 \mathrm{d}A = 2\pi \int_r^R r^3 \mathrm{d}r = \frac{2\pi}{4}\left(R^4 - r^4\right). \tag{12}$$

Combining Equations 10, 11 and 12 we can write down the force required to deflect the coils by an angle of 2°,

$$F = \frac{\theta G I_T}{L d} \approx 60\,\mathrm{N}, \tag{13}$$

where we used the geometry parameters $R = 1\,\mathrm{mm}$, $r = 0.75\,\mathrm{mm}$, $L = 3.5\,\mathrm{mm}$ and $d = 9.5\,\mathrm{mm}$.

Now we also need to know how much the axis will be deflected upon acting this force on it. This can be done using [9] the deflection of a beam mounted on one side,

$$f = \frac{FL^3}{3EI_X} \tag{14}$$

where the axial moment of inertia is for the given geometry $I_X = I_T/2$. The E module is given above. Therefore, the beam will be deflected by

$$d = 12\,\mu\text{m}.$$

These calculations strongly depend on the radii of the tube used. These are somewhat challenging to fabricate precisely as the length required of the tube is 14.5 mm, and its diameter is only 2 mm. This means that the lathe will not be very precise, as $L > 6r$. Therefore, these calculations give an estimation, but not absolutely precise values.

One problem that occurred later on was that the screws used to fix the BeCu tube in the bearings could not press it well enough against the walls, such that it would slip and yield a mechanical hysteresis. This problem can be somewhat tackled using pointy titanium screws that drill a bit into the tube. In order not to deform the tube upon tightening the screws, a rod that fills out the tube is placed inside the tube. Like this, an elastic tilting of $\approx 1.6°$ is achieved.

3.4 Final Design

The final design of the sample holder is shown in Figure 7. The main plate of the sample holder is connected to the cold stage with three elements. Two of them have extra big feet that make a better thermal contact. The third one can not be bigger due to spacial constrictions in the fridge. The mechanical axis is pressing with a micrometer screw on a titanium plate fixed at the coils to tilt them. The micrometer screw is guided in a part that is separately screwed to the cold stage.

The coils are mounted using only the BeCu tubes mentioned in section 3.3. Also shown are the additional thermalizations on the outside of the coil bodies. Further copper braids (not shown) can be mounted there). The sample lies on a PCB which is placed on the PCB holder and covered with another copper part. Together, these parts can then be slided inside to coils an screwed to the main plate. The RF ports are indicated with the SMP connectors.

For the temperature control, a temperature sensor and a heater are placed on the main plate. The heater is self built, we use a copper part with a hole inside and glue a 100 Ω resistor inside using Stycast. The temperature sensor is a calibrated Cernox sensor from Lakeshore. A silicon diode is not suited as its response depends on the magnetic field.

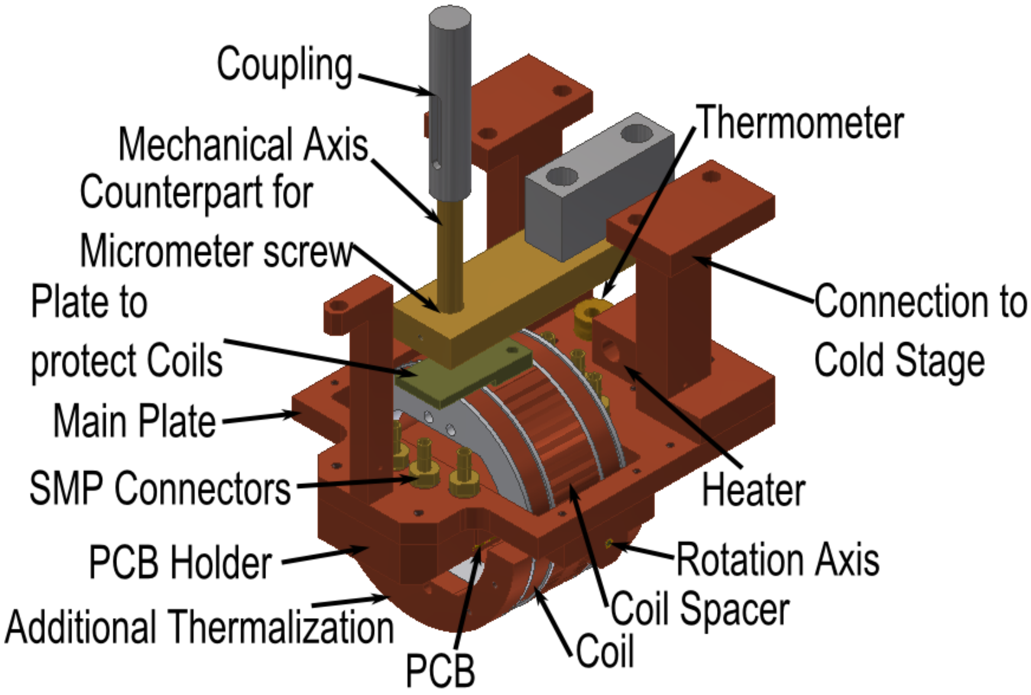

Figure 7: The final design of the sample holder. The sample will be placed on the PCB holder inside of the coils.

3.5 Improvement Suggestions for a Next Generation

Thermalization At this point, the thermalization seems to be too bad to sustain a current of more than 80 mA in the coils. If more current is sourced, the coils quench. This means, that they loose their superconducting properties, and become normal conductors. This can have several reasons.

First, it can be due to mechanical motion of the wires which leads to friction and therefore heating. This is something that will get better with every quench, as the wires adjust their positions towards a more favorable one with every bit of motion.

A second possibility is a defect in the material of the wire. This can be, as rather strong forces act on the wire when it is wound around the coil body. Material defects have the tendency to get worse with every quench, as the strong heating would rather lead to more damages than improvements.

A third possibility is the occurrence of the Kosterlitz-Thouless-Beresinzki transition, see Ref. [11] and section 8.2 of [12] which could apply to the present case as the wire is thin. Due to thermal fluctuations there is a spontaneous formation of vortex anti-vortex pairs. The formation of these pairs is enhanced as there is current flowing. These vortices are then pulled apart due to the Lorentz force acting on them, and lead again to dissipation. It could be reduced by lowering the initial temperature of the coils, as then fluctuations would be damped exponentially with lower temperature.

But what seems most likely is that the onset of resistance in type-II superconductors plays a role here, compare [12] section 5.5.2. Type-II superconductors have a gradual increase in resistance from a certain current on until they reach the normal state. As the maximum source-able current for a steady state operation increased with the quality of the thermalizations, this is most likely still the limiting factor.

A fifth problem could be a contact resistance in a solder joint connecting the superconducting wires with the copper wires. If there is a contact resistance, heat is generated there and gradually starts to destroy the superconducting phase in the wire.

Mechanics If the BeCu tubes are not machined properly, the spring constants change a lot. This can lead to a stiffer spring that leads earlier to mechanical hysteresis. Another problem is that the screws used to fix the position of the BeCu tube are only M2. That makes them rather fragile and it can happen that they break off. In a next iteration of the design if would be favorable to use M3 screws, as they are more robust.

RF Cabling The titanium protection plate of the coils is coming quite close over the SMP connectors for the RF cabling. That means that the RF cables of two ports need to be bent right after the end of the connector. This can lead to damages at the solder joint on the connector. This problem is eased if copper cables are used, as they are easier bendable.

4 Theoretical Models

The goal of this section is to derive an analytical expression that describes dissipation in a resonator due to an external magnetic field. We will start with a brief introduction to type-II superconductivity. Then, we will express the dissipation due to moving Abrikosov-vortices analytically. To do so, we will see that an expression for the current density and the magnetic field in the resonator is needed.

The main points this chapter discusses are:

- Introduction to superconductivity

- Derivation of an analytic expression describing the dissipation due to vortices in a superconducting coplanar waveguide resonator in a magnetic field
- Estimation of the power circulating in the resonator
- Estimation of the critical current density of the niobium strip used
- Current distribution models due to a transport current
- Current distribution models due to shielding currents induced by external magnetic fields
- Magnetic field in the resonator due to transport currents
- Magnetic field in the resonator due to external fields
- Discussion of the presented models
- Selection of feasible models

4.1 Brief Introduction to Type-II Superconductivity

In this section, we shall briefly revisit the basics of superconductivity, especially type-II superconductivity. We will follow References [12] and [13] for this. CGS units are used to stay in line with textbooks. This section does not aim to give a sound introduction to superconductivity but rather wants to remind the reader of all the important terms. Therefore, a basic understanding of superconductivity is a prerequisite.

London Equations Two years after the discovery of the Meissner-Ochsenfeld effect [14] the London brothers came up with a theory that describes several effects of superconductivity surprisingly well [15]. Their theory relies on the response of a perfect normal conductor to an electric field. The London equations are given as

$$\boldsymbol{E} = \frac{\partial}{\partial t}(\Lambda \boldsymbol{J}_S) \tag{15}$$

$$\boldsymbol{h} = -c\nabla \wedge (\Lambda \boldsymbol{J}_S) \tag{16}$$

where $\Lambda = \frac{4\pi\lambda^2}{c^2} = \frac{m}{n_S e^2}$ is a phenomenological parameter and n_S is the number density of superconducting electrons. They assume that n_S changes continuously from 0 at the critical field T_C to n at 0 K. The superconducting electrons then behave like a superfluid embedded in the normal conducting electrons. An important parameter that follows from this theory is the London penetration depth λ. If we apply the Maxwell equation$\nabla \wedge \boldsymbol{h} = 4\pi \boldsymbol{J}/c$ on Equation 16 we get

$$\nabla^2 \boldsymbol{h} = \frac{\boldsymbol{h}}{\lambda^2}. \tag{17}$$

This equation explanis the Meissner-Ochsenfeld effect, as it describes that a magnetic field is screened from the inside of a superconductor with a characteristic decay length of λ. The temperature dependence of the penetration depth can be approximately given as

$$\lambda_L(T) \approx \lambda_L(0)\sqrt{1 - \left(\frac{T}{T_C}\right)} \quad \text{with} \quad \lambda_L(0) = \left(\frac{mc^2}{4\pi n e^2}\right)^{1/2}$$

which suggests that $\lambda_L(T)$ diverges as $T \to T_C$ which is experimentally approved.

Coherence Length In the limit $T \to 0$, the experimental values for λ are always bigger than the theoretical ones of this formalism. This leads to the introduction of a new concept, the coherence length ξ_0.

The coherence length ξ_0 can be obtained from different ways. Pippard [16] obtained it using a non-local generalization of the expression of the London theory for the current. In the Bardeen-Cooper-Schrieffer theory [17], the coherence length enters the picture as the approximate separation of the electrons in a Cooper pair. However, for the purpose here it is more interesting to look at an other phenomenological theory, the Ginzburg-Landau theory.

The Ginzburg-Landau Theory The complex order parameter ψ describes the density of superconducting electrons as $|\psi|^2 = n_S$. The great achievement of Ginzburg and Landau was that they had the intuition to write down an expression for the free energy F of a superconductor close to its phase transition,

$$F = F_n + \alpha|\psi|^2 + \frac{\beta}{2}|\psi|^4 + \frac{1}{2m}|(-i\hbar\nabla - 2e\boldsymbol{A})\psi|^2 + \frac{|\boldsymbol{B}|^2}{2\mu_0},$$

where F_n is the free energy of the normal phase, α and β are temperature dependent phenomenological parameters. Equations for the current density and for ψ can then be obtained by minimizing the free energy with respect to fluctuations in ψ and $\boldsymbol{A}$.

Below the critical temperature of a superconductor, according to this theory, the density of superconducting electrons is given as

$$|\psi|^2 = -\frac{\alpha_0(T - T_C)}{\beta}$$

which is a typical behavior for second order phase transitions. The Ginzburg-Landau Equations then introduce a new length, the coherence length

$$\xi(T) = \frac{\hbar}{|2m^*\alpha(T)|^{1/2}}. \tag{18}$$

This length characterizes over which distance $\psi(\boldsymbol{r})$ can vary without significant increase in energy. This expression coincides with the expression Pippard found, but only for T far below T_C. The $\xi(T)$ in Equation 18 diverges at T_C as α vanishes with $(T - T_C)$.

The important parameter we obtain now is the Ginzburg-Landau parameter

$$\kappa = \frac{\lambda}{\xi} \tag{19}$$

which is approximately temperature independent. For superconductors that show a total Meissner-Ochsenfeld effect, κ is always below $1/\sqrt{2}$. In this case, the surface energy between the normal and superconducting phase is positive and one speaks of a *Type-I Superconductor*

Abrikosov Vortices However, if the Ginzburg-Landau parameter is larger than $1/\sqrt{2}$ (*Type-II Superconductor*), the energy of a surface between the normal conducting and the superconducting phase becomes negative. This means that it becomes favorable for the superconductor to have normal conducting regions inside it. If the superconductor is placed in a magnetic field, it is then - above a critical field - penetrated by flux tubes. Abrikosov called this flux tubes vortices. The center of these vortices is normal conducting, and they are threaded by a magnetic flux of one flux quantum $\Phi_0 = h/2e$. Upon increasing the applied field this goes on until an upper critical field where the superconducting properties vanish.

4.2 Current Dissipation due to Abrikosov-Vortices

It is helpful to first get an understanding of the forces acting on a vortex in our setup. We consider the geometry shown in Figure 8 and use from now on the SI unit system. A long superconducting strip of thickness d, length l and width S is in an external magnetic field $\boldsymbol{B} = B \cdot \hat{e}_z$ perpendicular to the

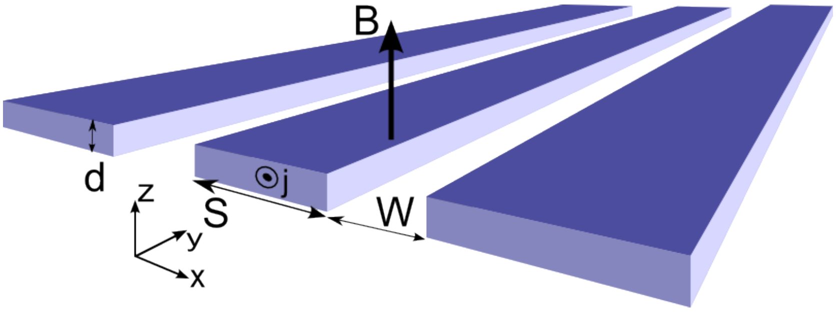

Figure 8: The geometry of the considered situation. It is a superconducting coplanar waveguide, with center conductor width S, film thickness d and gap size W.

strip. The strip is threaded by a current density $\boldsymbol{j}(x, z, t) = j(x, y, z, t) \cdot \hat{e}_y$. The current is a standing wave in the resonator, and because there can not be any current flowing at the very ends of the resonator there is a $\sin(y\pi/l)$-dependence in y-direction. The time dependence of the standing wave is given as $\sin(t \cdot 2\pi f_{Res})$. Therefore, the total current density can be written as

$$\boldsymbol{j}(x, y, z, t) = j(x, z) \sin(y\pi/l) \sin(t \cdot 2\pi f_{Res}) \hat{e}_y. \tag{20}$$

Now we look at the behavior of the vortex in a superconductor that carries a current. As the vortex is threaded by a magnetic field and a current is flowing around it, a Lorentz force $\boldsymbol{F_L}$ acts on the system,

$$\boldsymbol{F_L} = q \cdot \boldsymbol{v} \wedge \boldsymbol{B}.$$

Lets consider the force acting on one vortex, $\boldsymbol{f_L}$. We can express $q \cdot \boldsymbol{v}$ as the current density $\boldsymbol{j}(x, y, z, t)$. To balance the equation, we need to replace the magnetic field by the flux density. As a vortex carries exactly one flux quantum $\Phi_0 = h/2e \approx 2.07 \cdot 10^{-15}$ Wb, the force per vortex is then given by

$$\boldsymbol{f_L} = \boldsymbol{j}(x, y, z, t) \wedge \boldsymbol{\Phi_0} = j(x, y, z, t)\Phi_0 \cdot \hat{e}_x \tag{21}$$

for the geometry of used in Figure 8.

Another force acting on a vortex arises when the vortex is moving. Phenomenologically, one can describe it as a viscous force $\boldsymbol{f_R}$ resisting the motion of a vortex [12]. We call the drag coefficient η, and as a vortex moves with velocity $\boldsymbol{v}$, the force

$$\boldsymbol{f_R} = -\eta \boldsymbol{v} \tag{22}$$

acts on it. Note that this force does *not* account for a complete pinning of vortices, but only a viscous damping of their motion. The implicit assumption is that the vortices hop from one pinning center to another, which can be described by a viscous motion. A more detailed analysis would be required if an explicit pinning potential should be considered.

The viscous drag coefficient η is given as [12, 18, 19]

$$\eta = \frac{\Phi_0^2}{2\pi a^2 c^2 \rho_n}\ _{[CGS]} \quad \approx \frac{\Phi_0 H_{C_2}}{\rho_n c^2}\ _{[CGS]} \quad = \frac{B_{C_2}\Phi_0}{\rho_n}\ _{[SI]} \tag{23}$$

where the indices $[CGS]$ and $[SI]$ stand for the unit system the expression is written in, a denotes the core diameter of the vortex (we assume $a \approx \xi$, with ξ the coherence length of the superconductor), c is the speed of light and ρ_n is the normal state resistivity of the superconducting material.

To get the equation of motion for the vortex, we need to add the forces in Equations 21 and 22 and set them to zero. As the Lorentz force only acts in the x-direction, $\boldsymbol{v}$ will also point in x-direction, therefore

$$\boldsymbol{f_L} + \boldsymbol{f_R} = 0 \Leftrightarrow j(x,y,z,t)\Phi_0 = \eta v. \tag{24}$$

The energy dissipated due to the viscous motion of one vortex ΔE per cycle of duration $T = 2\pi/\omega$ is given as [20]

$$\Delta E = \int_0^T f_L v \mathrm{d}t \overset{\text{Eq. 21, 24}}{=} \frac{\Phi_0^2}{\eta}\int_0^T j^2(x,y,z,t)\mathrm{d}t. \tag{25}$$

The total dissipated energy ΔE_{tot} is the sum of all the energies ΔE_i dissipated by the individual vortices,

$$\Delta E_{tot} = \sum_i \Delta E_i. \tag{26}$$

Assuming strong magnetic fields, respectively many vortices per unit area, we can think about a continuous vortex density $n(x,y)$. The vortex density is given as

$$n(x,y) = \frac{|B(x,y)|}{\Phi_0}. \tag{27}$$

This allows us to express Equation 26 in a continuous manner,

$$\Delta E_{tot} = \frac{\Phi_0^2}{\eta}\int_0^T \int_V j^2(x,y,z,t)\cdot n(x,y,t)\mathrm{d}\boldsymbol{r}\,\mathrm{d}t, \tag{28}$$

where $\mathrm{d}\boldsymbol{r} = \mathrm{d}x\,\mathrm{d}y\,\mathrm{d}z$ and the integration is performed over the whole volume V of the strip. Using Equation 27 we can rewrite the total energy dissipated per cycle in terms of the magnetic field in the superconducting strip and the current density that threads it,

$$\Delta E_{tot} = \frac{\Phi_0}{\eta} \int\limits_0^T \int\limits_V j^2(x, y, z, t) \cdot |B(x, y, t)| \mathrm{d}\boldsymbol{r} \, \mathrm{d}t. \tag{29}$$

Let's now assume that the external magnetic field is uniform. This makes the y-dependence in Equation 27 vanish, because the reaction of the superconducting resonator to an external field will be the same for all y values, it only depends on x. This is of course not entirely true as at the end of the resonator we expect edge effects. Because the resonator is long, this will have a negligible influence. Also, we observe the situation for static magnetic fields, therefore B does not have a time dependence. Thus, we can perform two integrals in Equation 29, using the current dependence of Equation 20 and the Fubini rule

$$\begin{aligned} \Delta E_{tot} =& \frac{\Phi_0}{\eta} \int\limits_0^T \sin^2(t \cdot 2\pi f_{Res}) \mathrm{d}t \cdot \int\limits_0^l \sin^2(y \cdot \pi/l)) \mathrm{d}y \cdot \\ & \cdot \int\limits_{-d/2}^{d/2} \int\limits_{-S/2}^{S/2} j^2(x, z) \cdot |B(x, y)| \mathrm{d}x \, \mathrm{d}z \\ =& \frac{\Phi_0 l}{4\eta} \int\limits_{-d/2}^{d/2} \int\limits_{-S/2}^{S/2} j^2(x, z) \cdot |B(x, y)| \mathrm{d}x \, \mathrm{d}z. \end{aligned} \tag{30}$$

In order to compare these theoretically calculated losses to the measured losses, it is necessary to get an understanding of the description of losses in a resonator. The resonator used can be described as a driven harmonic oscillator. In the frequency space, the response function of a driven harmonic oscillator is a Lorentzian,

$$\mathcal{L}(a, b, f, f_{Res}, \Delta f) = A + \frac{B \Delta f^2}{(f - f_{Res})^2 + \Delta f^2}, \tag{31}$$

where A and B are constants that are not important for now, f_{Res} is the resonance frequency of the oscillator, f is the frequency and Δf is the peak width. A more meaningful quantity describing the resonator is the quality factor Q. Using the parameters of Equation 31 we can express it as

$$Q = \frac{f_{Res}}{\Delta f}. \tag{32}$$

The quality factor is basically a measure for how often a photon is reflected in the resonator until it is coupled out or lost. It will be dependent on the magnetic field, $Q = Q(B)$.

The peak width can be expressed as a sum of losses, the internal γ and the external κ losses of the resonator. We will observe that the peak width will increase with an applied magnetic filed B. We can assume that the external losses are not dependent on the magnetic field, but the internal losses will be. This is due to the vortex movement described above. Thus, we can rewrite Equation 32 to

$$Q(B) = \frac{f_{Res}}{2\kappa + \gamma_0 + \gamma(B)} \tag{33}$$

where we split γ in a field independent part γ_0 and a field dependent part $\gamma(B)$. In our analysis we will not use this form of the equation, it is just displayed for the sake of completeness.

One can also think of the quality factor as being the ratio of the energy stored in the resonator and the energy lost per cycle,

$$Q(B) = 2\pi \frac{\text{Energy Stored}}{\text{Energy Dissipated per Cycle}} \overset{\text{Eq. 30}}{=} \frac{2\pi}{f_{Res}} \frac{P_{Stored}}{\Delta E_{tot}} \tag{34}$$

where again $\Delta E_{tot} = \Delta E_{tot,0} + \Delta E_{tot}(B)$. In our analysis we will compare the inverse of the measured quality factor with the total dissipated energy,

$$\frac{1}{Q(B)} = \frac{\Delta E_{tot,0} f_{Res}}{2\pi P_{Stored}} + \frac{\Delta E_{tot}(B) f_{Res}}{2\pi P_{Stored}}, \tag{35}$$

because this quantity is easiest to fit. In this equation, the term $1/Q(B)$ is obtained by inverting each point of the measured data. Also, f_{Res} is obtained from the measurement. An estimation for the stored power in the resonator, P_{Stored} will be given in the next section. The constant $\Delta E_{tot,0}$ is obtained by the condition that there are no losses due to the magnetic field at zero field are. The $\Delta E_{tot}(B)$ is the quantity we try to fit, using different models.

4.3 Measurement of the Power in the Resonator

Now, we try to get an estimation of the order of magnitude of the current in the resonator. For this we will follow the method used in Ref. [21]. Oates et. al. calculate the circulating power in the resonator and deduce from it the maximum current in the resonator.

For the measurement, a Vector Network Analyzer (VNA) is used. This device measures the frequency dependent S-parameters [22]. The measured data is displayed in Figure 9. Blue and green indicate reflections S_{11} and

S_{22}, red and yellow are transmissions S_{12} and S_{21}. The VNA is set to send a power of -15 dBm into the system. The signal is attenuated by the cables (5.5 dB) and on the port 1 side of the resonator by a 20 dB attenuator. This explains why the green reflection curve (S_{22}) shows a dip and the blue does not. The green curve shows the reflection at the resonator, the blue curve is dominated by the reflection at the attenuator and is therefore damped. Similarly, the transmission S_{21} in yellow shows a nonlinearity, because it has a too high incident power on the resonator. The transmission from port one to port two does not show this feature, as it is damped before reaching the resonator. Its incident power on the resonator is

$$P_{in} = (-15 - 5.5 - 20)\,\mathrm{dBm} = -40.5\,\mathrm{dBm} = 8.9 \cdot 10^{-8}\,\mathrm{W}.$$

The power at the output of the resonator can be calculated from the transmission measurement done with the VNA, shown in Figure 9, red curve. The transmission at the resonance frequency is damped by 32.4 dB with respect to the -15 dBm sent into the system. The attenuation due to the cables is 6.5 dB. Therefore, the power at the output of the resonator is

$$P_{out} = (-15 - 32.4 + 6.5)\,\mathrm{dBm} = -40.9\,\mathrm{dBm} = 8.1 \cdot 10^{-8}\,\mathrm{W}.$$

The quality factor of the resonator is

$$Q = \frac{f_{res}}{\Delta f} = 60‘000$$

and the reflection coefficient r is given as

$$r = \sqrt{P_{out}/P_{in}}.$$

With these tools we can express the stored power P_{Stored} as

$$P_{Stored} = 4P_{in} r(1-r)Q/\pi = 2.9 \cdot 10^{-4}\,\mathrm{W}.$$

As the quality is high, the circulating power is mostly reactive. Therefore the current I in the resonator is given as

$$I \approx \sqrt{P_{Stored}/\left(2\pi f_{res} L\right)}, \tag{36}$$

where L is the total inductance of the resonator. It can be calculated from the line inductance L' with

$$L = 2L' \cdot l/\pi^2, \tag{37}$$

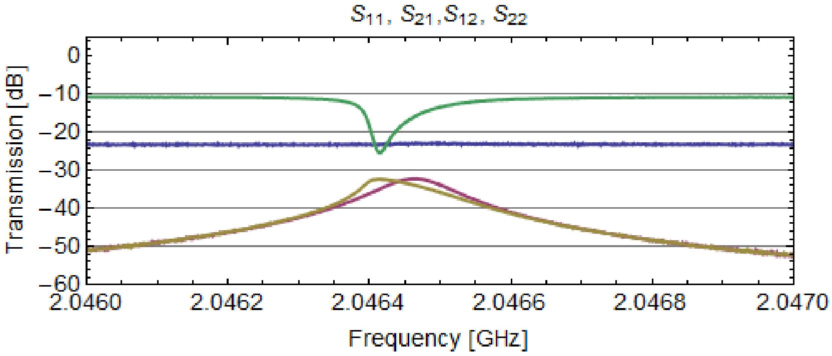

Figure 9: VNA data around the transmission peak of the resonator. Green and Blue are reflections, Red and Yellow are transmissions.

where l is the length of the resonator.The characteristic impedance Z_0 of the resonator is

$$Z_0 = \sqrt{\frac{L'}{C'}} = 50\,\Omega, \tag{38}$$

with C' being the line capacitance. The phase velocity v_ϕ depends on the effective dielectric constant ε the resonator feels,

$$v_\phi = \frac{c}{\sqrt{\varepsilon}} = \frac{1}{\sqrt{L'C'}}. \tag{39}$$

The dielectric constant can be obtained from the wave equation

$$\lambda f_{res} = v_\phi$$

when the half-wavelength resonator condition, $l = \lambda/2$ is fulfilled. For the resonator length of $l = 3.2 \cdot 10^{-2}\,\mathrm{m}$ this leads to

$$\varepsilon = \left(\frac{c}{2 f_{res} l}\right)^2 = 5.5\,.$$

Using Equations 38 and 39 we get the line inductance

$$L' = \frac{Z_0}{v_\phi} = \frac{Z_0\sqrt{\varepsilon}}{c} = 3.9 \cdot 10^{-7}\,\mathrm{H/m}. \tag{40}$$

This is in agreement with a geometrical derivation of L' as in [23], where

$$L' = \frac{\mu_0}{4}\frac{K\left(\sqrt{1-\frac{S}{S+2W}}\right)}{K\left(\frac{S}{S+2W}\right)} = 3.6 \cdot 10^{-7}\,\mathrm{H/m}, \tag{41}$$

with K being the complete elliptic integral of the first kind and W the distance between resonator and ground plane.

Therefore, the total inductance of the resonator can be calculated by using Equation 37 and 40 to be

$$L = 2.5\,\mathrm{nH}. \tag{42}$$

With Equation 36 it follows that the total current in the resonator is

$$I = 3.0 \cdot 10^{-3}\,\mathrm{A} = 3\,\mathrm{mA}. \tag{43}$$

This result has to be taken with care. For example, the attenuation of the cables is only measured at room temperature. But the measurement is performed in liquid helium. This temperature difference will change the attenuation of the cables. Therefore, the estimations made for the incident power are not very precise. Already small changes in the incident power will lead to large changes in the estimated current in the resonator. Thus, Equation 43 should rather be considered as an order of magnitude result.

4.4 Estimation of the Critical Current Density

We are interested in the critical current density j_{Crit} of our niobium films. It is not entirely easy to estimate the correct j_{Crit} as it not only depends on the material but also on the geometry. We will use three different approaches to get an estimation of how precise we can determine it. First, we can consider literature values for niobium films of thickness $1\,\mu$m. The current density for films of width $10\,\mu$m (the width of our resonator) is $j_{Bulk} \approx 3-4.5 \cdot 10^{10}\,\mathrm{A/m^2}$ [24], depending on the substrate temperature during the film deposition. These results are obtained at a temperature of 4.2 K.

To get a second value, we can use the critical magnetic field of niobium and convert it into a current density, using equation (5.61) in [13]

$$j_{Crit} = \frac{2\sqrt{2}B_{Crit}(0)}{3\sqrt{3}\mu_0\lambda_L(0)}\left(1-\frac{T}{T_C}\right)^{\frac{3}{2}}. \tag{44}$$

Using the value from [13] for $B_{Crit}(0) = 0.18\,\mathrm{T}$, from [25] for $\lambda_L(0) = 100\,\mathrm{nm}$ and $T_C = 8.67\,\mathrm{K}$ from [23] we get for $j_{Crit}(T = 4.2\,\mathrm{K}) = 1.2 \cdot 10^{12}\,\mathrm{A/m^2}$.

A third method is to obtain j_{Crit} is measuring it. This was not done during this thesis, but a former member of the group, Gabriel Puebla-Hellmann, did this. He used a $S = 10\,\mu$m wide, 150 nm thick niobium strip without holes in liquid Helium (4.2 K) and got a critical current of 25-30 mA [26]. This yields a current density of

$$j_{Crit} = \frac{I}{S \cdot d} = \frac{30\,\mathrm{mA}}{10 \cdot 0.15\,\mu\mathrm{m}^2} = 2 \cdot 10^{10}\,\mathrm{A/m^2}. \tag{45}$$

The big spread of these numbers shows that it would be helpful to measure the critical current density directly in order to get an actually useful value.

For further calculations we will use this last value because its parameters are the same as the ones in our resonator. They should be used with care though, as some of the resonators we use have holes in the center conductor.

4.5 Superconducting Current Density Models

In the expression for the dissipation in a resonator in an external magnetic field due to Abrikosov vortices, Equations 30 and 35, we have seen that we need a description of the current density in the resonator. We will discuss five different models that can be used to describe the current density distribution. The most essential distinction is that the first three of the presented models describe the current density in the resonator due to a transport current within the resonator. The last two describe a current density that arises as shielding currents due to an externally applied field. Later on, we will discuss that with our setup we are insensitive to losses due to shielding currents, as these are powered by the external field.

The Constant Current Model The easiest possible model for the current density in the resonator due to a transport current is a constant current density. We can just take the value given in Equation 45 that results from a measurement on a comparable niobium strip with the same geometry parameters as ours. Although, care needs to be taken as we use some resonators that have holes in the center conductor. The value used for further estimations is $2 \cdot 10^{10}\,\mathrm{A/m^2}$.

LW approximation of exact flux-free current distribution Lahl and Wördenweber (LW) [27] use that the current distribution in a flux free superconducting coplanar waveguide resonator due to an applied transport current I_a can be approximated by

$$\boldsymbol{j}_{RF}(x,y,z,t) = j_{RF}(x) \cdot \hat{e}_y = \frac{I_a}{K(\frac{S}{S+2W})d \cdot S\sqrt{\xi(x)}} \cdot \hat{e}_y \tag{46}$$

where $K(\frac{S}{S+2W})$ denotes the complete elliptic integral of the first kind, $W = 5\,\mu\mathrm{m}$ is the distance between the resonator and the ground plane and $\xi(x)$ is given as

$$\xi(x) = \begin{cases} \frac{\lambda_{eff}}{S}\left[1-\left(\frac{S}{S+2W}\right)^2\right], & \text{for } 0 \leq \frac{S}{2} - |x| < \lambda_{eff} \\ \left[1-\left(\frac{2x}{S}\right)^2\right]\left[1-\left(\frac{2x}{S+2W}\right)^2\right], & \text{for } |x| \leq \frac{S}{2} - \lambda_{eff}, \end{cases}$$

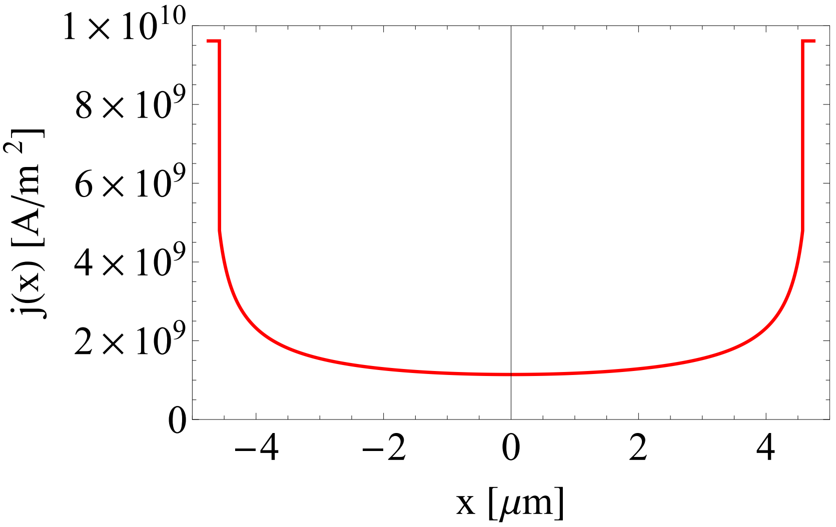

Figure 10: Current density distribution over the strip from Equation 46. The parameters used are given in the text.

where $\lambda_{eff} = \lambda_L \coth(d/\lambda_L)$ is the effective penetration depth calculated from the London penetration depth λ_L. The temperature dependence of the penetration depth is given by Equation (12.5b) in [28],

$$\lambda_L(T) = \lambda_L(0)\,(1 - T/T_C)^{-1/2}\,, \tag{47}$$

where the parameter $\lambda_L(0)$ is the London penetration depth at 0 K. There are different sources for the London penetration depth of Niobium. Abdumalikov et. al. [25] find $\lambda_L(0) = 100$ nm for a strip geometry. In [13] different sources are named, they state values of 32 nm, 39 nm and 85 nm.

The current distribution in this model therefore depends on the geometry, the London penetration depth (therefore the material) and the temperature. The current density plotted over the width of the strip is shown in Figure 10. It can be seen that the current density is very strong around the edges of the strip, and almost negligible towards the center.

The NBI Current Density Model due to Transport Currents The model by Norris, Brandt and Indenbom (NBI) [29,30] assumes a strip of hard superconducting material being placed in a perpendicular magnetic field, as in Figure 8. They use an important idea of Bean, [31,32] who was one of the first to come up with a hysteresis model for the discussed situation. The idea is that there can not be a current density higher than j_{Crit} in the strip. But it is not the case anymore that the current density itself is noncontinuous, only it's first spacial derivative. There are two cases of the model, namely the current density distribution due to a transport current in the strip and the current density due to an externally applied magnetic field which we will discuss later. In both cases, a hysteresis can be observed when the direction of the transport current, respectively the magnetic field, is reversed.

Let's first consider the current distribution in the strip when there is a transport current I_a being sourced. According to Ref. [30] it is given as

$$j(x, I_a) = \begin{cases} \frac{2j_{Crit}}{\pi} \arctan\left(\frac{\left(\frac{S}{2}\right)^2 - b^2(I_a)}{b^2(I_a) - x^2}\right), & |x| < b(I_a), \\ j_{Crit}, & b(I_a) < |x| < \frac{S}{2}, \end{cases} \tag{48}$$

where $b(I_a)$ is the penetration depth of the magnetic field due to the transport current I_a,

$$b(I_a) = \frac{S}{2}\sqrt{1 - \frac{I_a^2}{I_{Crit}^2}}. \tag{49}$$

Here, I_{Crit} is the maximal current the strip can carry, $I_{Crit} = j_{Crit} \cdot S \cdot d$. This is shown in Figure 11. In our case, the current ratio I_a/I_{Crit} can be obtained using Equations 43 and 45 to be

$$\frac{I_a}{I_{Crit}} = \frac{3\,\mathrm{mA}}{28.5\,\mathrm{mA}} = 0.11. \tag{50}$$

The current distribution for this value is indicated blue in Figure 11.

The current distribution is dependent on the history of the transport current through the strip. If a current I_0 was sourced, which is higher than all the previously sourced currents, only this current determines the current distribution throughout the strip and is given by Equation 48. If the transport current I_a then is reduced, the hysteretic current density $j^{\downarrow}(x, I_a, I_0)$ is given as (compare Equation 55)

$$j^{\downarrow}(x, I_a, I_0) = j(x, I_0) - 2j\left(x, \frac{I_0 - I_a}{2}\right). \tag{51}$$

The hysteresis is shown in Figure 12. There, a maximal current $I_0 = 0.8\, I_{Crit}$ is applied. It is then stepwise reduced to $-I_0$. It can be seen that the edges of the strip change the fastest. As the final current is sourced, the previous maximum $+I_0$ has no influence on the current density distribution any more. The current density distribution is then again given by Equation 48.

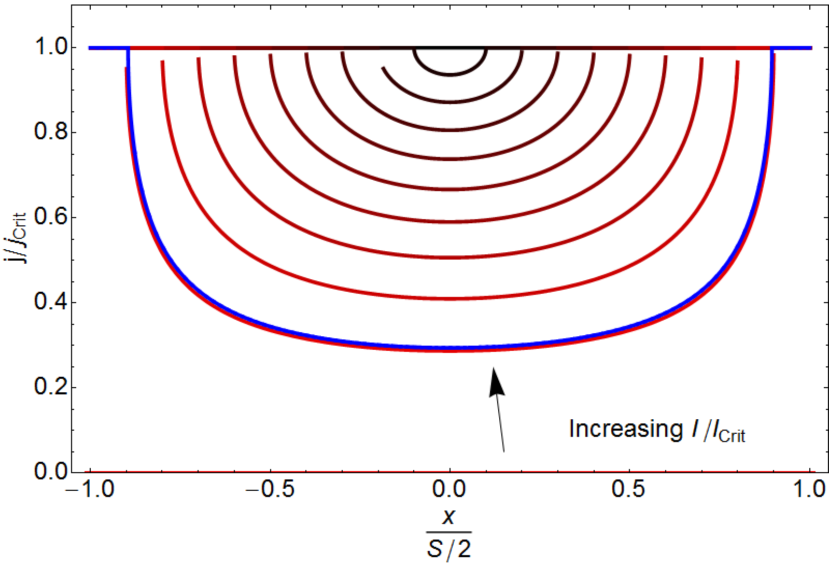

Figure 11: Current density distribution over the strip for different total currents through the strip. The ration of I_a to I_{Crit} is increased in steps of 0.1. The blue line is for a current ratio of 0.11.

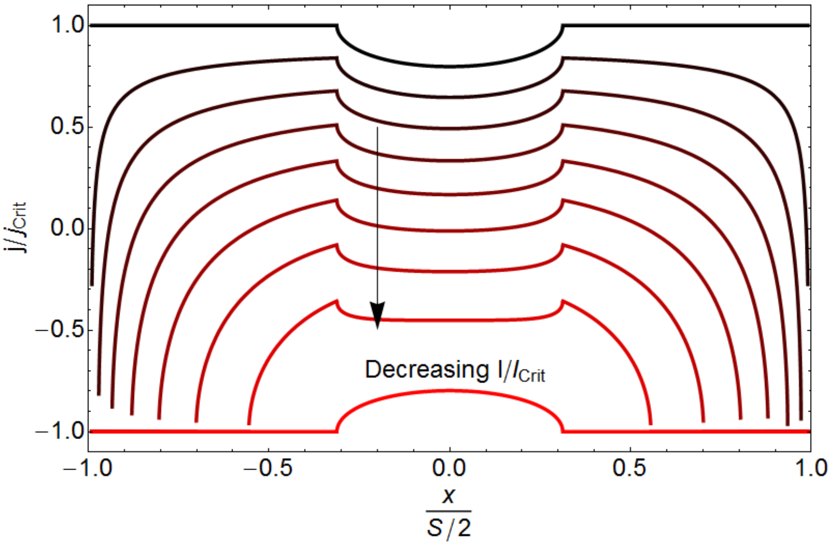

Figure 12: Current density distribution hysteresis. The initial state is due to a current of 0.8 I_{Crit}, and in the following curves the transport current is stepwise reduced to -0.8 I_{Crit}.

Bean Critical Current Density Model Let's now consider models for the current distribution due to an externally applied field. The field will induce shielding currents in the superconductor (compare the Meissner effect) and therefore lead to a nonzero current density. Bean considers a model where a superconducting material is placed in an external magnetic field $\boldsymbol{B}_{ext}$ and the material responds to this field due to the Maxwell equation

$$\boldsymbol{\nabla} \wedge \boldsymbol{B} = \mu_0 \boldsymbol{j} \tag{52}$$

where the electric field is assumed to be zero. The simplest current distribution model that takes an external magnetic field $\boldsymbol{B}_{ext}$ into account is the Bean critical state model. It assumes a infinite sheet of superconducting material in a parallel field (the geometry for this model is not the same as in Figure 8). This field makes the currents in the superconductor flow parallel to the surface of the superconductor. The superconductor is assumed to be hard, that means it is a type II superconductor with high pinning force. It shows diamagnetic behavior in an externally applied magnetic field. If the applied field B_a is weaker than the lower critical field, $B < B_{C_1}$, the Meissner effect occurs.

But for the case $B_{C_1} < B_a < B_{C_2}$ a critical current flows also below the surface. The model assumes that the current density in the superconductor due to the field is either the critical current density of the superconductor, or zero. Therefore, the current density distribution over the height of the sheet is such that is $+j_C$ for a slab of certain thickness, then 0 for a region in the middle of the sheet, and on the other side of the sheet is $-j_C$, compare Figure 13a.

Formally, this current distribution can be written as

$$j(z, B_a) = \begin{cases} j_C \frac{z}{|z|}, & \frac{d}{2} - |z| < \frac{10|B_a|}{4\pi j_C \mu_0}, \\ 0, & \frac{d}{2} - |z| \geq \frac{10|B_a|}{4\pi j_C \mu_0}. \end{cases} \tag{53}$$

If a field is applied that is too strong to be expelled from the superconducting strip, the current density distribution will be $+j_C$ in the upper half of the strip, and $-j_C$ in the lower half. The magnitude of this field is called the Bean critical field B_{Bean}, and it is given as [31, 32]

$$B_{Bean} = \frac{\pi \mu_0}{5} j_{Crit} \cdot d \tag{54}$$

for a strip of thickness d. In our case, this yields a field of 2.4 mT. Note that this current model can describe hysteresis, as shown in Figure 13b. There, a magnetic field of 2 mT is applied, and then reduced to 1 mT. This leads

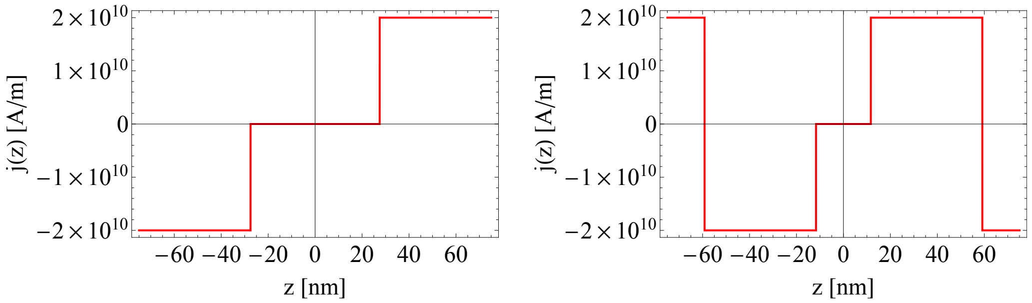

(a) An external field of 1.5 mT was applied to the virgin strip.

(b) First, a field of 2 mT was applied and then reduced to 1 mT.

Figure 13: Current distribution across the resonator according to the Bean model. Note that the figures do not show a cut along the x-direction of Figure 8 but along the z-direction.

to a sheet of current in the topmost layer of the sheet to flow in the reverse direction than before.

The hysteresis of the current, $j^{\downarrow}(z, B_a, B_{Max})$, which depends on the maximal applied field B_{Max} and the present field is described by

$$j^{\downarrow}(z, B_a, B_{Max}) = j(z, B_{Max}) - 2 \cdot j\left(z, \frac{B_{Max} - B_a}{2}\right). \tag{55}$$

The NBI Current Density Model due to an External Field We have already seen in the Bean critical state model that an external magnetic field leads to currents in the superconducting material. Norris, Brandt and Indenbom derived an analytical expression for this in a strip geometry in a perpendicular field (again, the geometry of Figure 8). They state that the current density distribution in the superconducting strip due to an externally applied magnetic field B_a is given as [30]

$$j(x, B) = \begin{cases} \frac{2j_{Crit}}{\pi} \arctan\left(\frac{C(B_a)\cdot x}{\sqrt{b(B_a)^2 - x^2}}\right), & |x| < b(B_a) \\ j_{Crit}\frac{x}{|x|}, & b(B_a) < |x| < \frac{S}{2}. \end{cases} \tag{56}$$

Here, the penetration depth $b(B_a)$ of the magnetic field is given as

$$b(B_a) = \frac{S}{2} \cosh\left(\frac{B_a}{B_{Crit}}\right) \tag{57}$$

and the function $C(B_a)$ is

$$C(B_a) = \tanh\left(\frac{B_a}{B_{Crit}}\right). \tag{58}$$

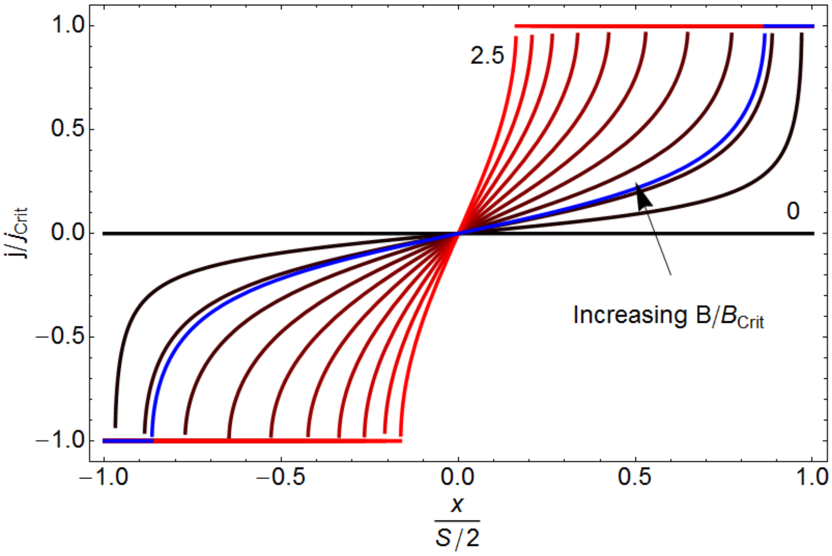

Figure 14: Current density distribution in a superconducting strip due to a perpendicular magnetic field. The magnetic field is increased from 0 to 2.5$\cdot B_{Crit}$ in steps of 0.25$\cdot$ B_{Crit}. The blue line is for a field ratio of 0.55.

The critical field can be obtained from the current density using equation 44 which yields $B_{Crit}(0) = 12\,\text{mT}$ if we use the critical current density of $2 \cdot 10^{10}\,\text{A/m}^2$ at T=4.2 K. Using Equation (2.56) in [13],

$$B_{Crit}(T) = B_{Crit}(0)\left[1 - \left(\frac{T}{T_{Crit}}\right)^2\right], \tag{59}$$

we get $B_{Crit}(T) = 9.5\,\text{mT}$. The current density distribution for this situation is shown in Figure 14. If we have a 0.3 T strong field that is misaligned by 1°, the perpendicular component of this field is $0.3 \cdot \sin(1°)\,\text{T} = 5.5\,\text{mT}$. The ratio B/B_{Crit} of this field is then 0.55. The blue line in Figure 14 displays the current density due to such a field.

As in the previous model, any maximum in the external field will erase the memory of the superconducting strip, and $j(x, B_a)$ is given by Equation 56. A hysteresis arises when an externally applied field B_a is applied that is lower than a previous field B_0. Then, the hysteretic current density distribution is given as

$$j^{\downarrow}(x, B_a, B_0) = j(x, B_0) - 2j\left(x, \frac{B_0 - B_a}{2}\right). \tag{60}$$

This behavior is shown in Figure 15. A magnetic field $B_a = 2\,B_{Crit}$ is applied, and then successively reduced to -2 B_{Crit}. One can clearly see that the

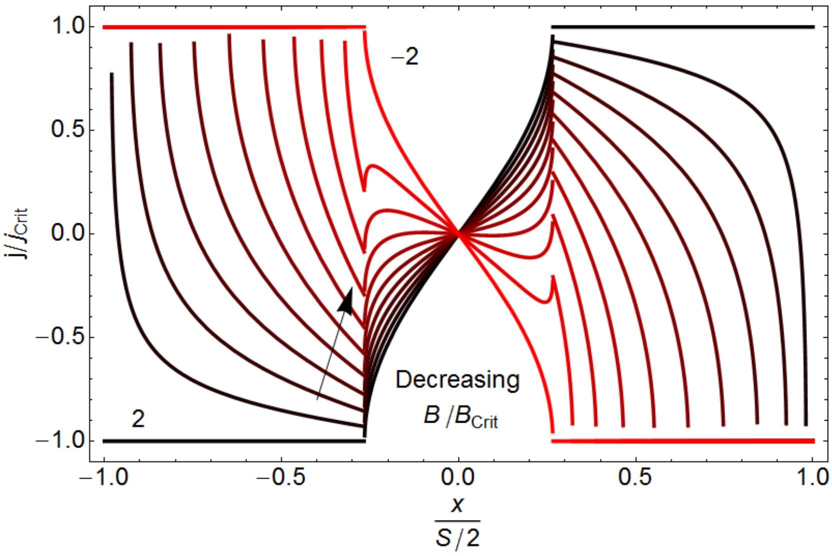

Figure 15: Current density distribution hysteresis. The initial state is due to an external field $B_a = 2\,B_{Crit}$, and in the following curves the external field is stepwise reduced to -2 B_{Crit}.

changes are fastest on the edge of the strip. Also, the memory of the current density distribution of the applied field vanishes as the applied field reaches a maximum again at $B_a = -2\,B_{Crit}$.

4.6 Models for the Magnetic Field in the Resonator

In order to calculate the dissipation due to vortices, we need an expression for the magnetic field in the resonator, see Equation 30. We will discuss three models describing the behavior of the magnetic field in the resonator. Again, we will make the distinction between fields that arise due to a transport current, and fields that arise due to an externally applied field. Later on, we will argue that the field inside a resonator due to a transport current does not contribute to the external field dependent losses $\Delta E_{tot}(B)$ in Equation 35. This is because they can be accounted for in $\Delta E_{tot,0}$ as this field stays the same, independent of the external field. Therefore, we will be mostly interested in the field distributions due to an externally applied field B_a.

The NBI Field Model due to a Transport Current Here, we will use again the geometry mentioned in Figure 8 and discuss the magnetic field in a superconducting strip arising from a transport current, [30]. The assumptions to the model are the same as in the paragraph above that discusses the current density in a superconducting strip due to a transport current. As in the Bean model, there is a region in the resonator where there is no magnetic field - provided that the applied transport current I_a is low enough. In and around the resonator the magnetic field is given as

$$B(x, I_a) = \begin{cases} 0, & |x| < b(I_a), \\ \frac{B_{Crit} x}{|x|} \operatorname{arctanh}\left[\left(\frac{x^2 - b^2(I_a)}{\left(\frac{S}{2}\right)^2 - b^2(I_a)}\right)^{\frac{1}{2}}\right], & b(I_a) \leq |x| < \frac{S}{2}, \\ \frac{B_{Crit} x}{|x|} \operatorname{arctanh}\left[\left(\frac{\left(\frac{S}{2}\right)^2 - b^2(I_a)}{x^2 - b^2(I_a)}\right)^{\frac{1}{2}}\right], & |x| > \frac{S}{2}, \end{cases} \tag{61}$$

where $b(I_a)$ is again defined as in equation 49 and

$$B_{Crit} = \frac{j_{Crit} \mu_0 d}{\pi} = 1.2\,\mathrm{mT}. \tag{62}$$

The dependence on the arctanh(ξ) function comes from using the equality $\operatorname{arctanh}(\xi) = \ln(|(1+\xi)/(1-\xi)|)$ and the latter emerges from an integration of the current density in Equation 48 according to amperes law. The magnetic field is plotted for various transport currents in Figure 16. The field resulting from the transport current we obtained in Equation 43 is indicated by the blue curve. Near the edges of the strip, a *logarithmic* singularity appears. This means that we will still be able to integrate it later on.

The hysteresis resulting from a reversion of the transport current is given by

$$B^{\downarrow}(x, I_a, I_{Max}) = B(x, I_{Max}) - 2 \cdot B\left(x, \frac{I_{Max} - I_a}{2}\right) \tag{63}$$

where I_{Max} denotes the maximal transport current and I_a is the current to a later time. In Figure 17 a current $0.9 \cdot I_{Max}$ is applied and then reduced to $-0.9 \cdot I_{Max}$. The fastest changes occur on the edge of the strip, but gradually also the regions inside change the field direction.

Bean Field Model We again use the same geometry as in the Bean model for the current [31,32]. It is a superconducting sheet in an externally applied magnetic field B_a that is parallel to the surface. The currents that were discussed in the Bean model before now araise again and reduce the field as it penetrates the superconductor. Because there is a constant current density, the field in the superconductor B_{In} will decrease linearly as

$$B_{In}(z, B) = \begin{cases} \frac{2B_{Bean}}{d}|z| - (B_{Bean} - B), & \frac{d}{2} \geq |z| > \frac{d}{2}\left(1 - \frac{B}{B_{Bean}}\right), \\ 0, & |z| \leq \frac{d}{2}\left(1 - \frac{B}{B_{Bean}}\right), \end{cases} \tag{64}$$

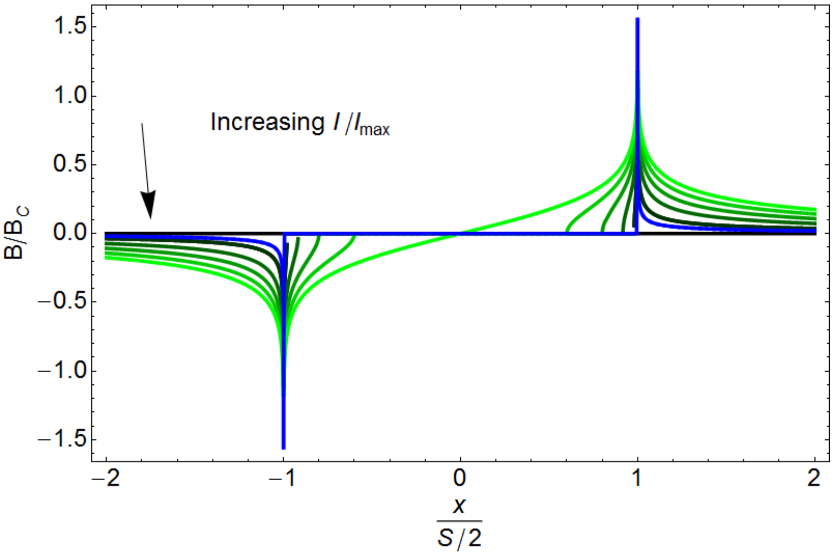

Figure 16: The magnetic field resulting from a transport current in the superconducting strip. The current is increased from 0 to I_{Max} in steps of $0.2 \cdot I_{Max}$. Note that the x-axis of the figure ranges further than just the width of the strip.

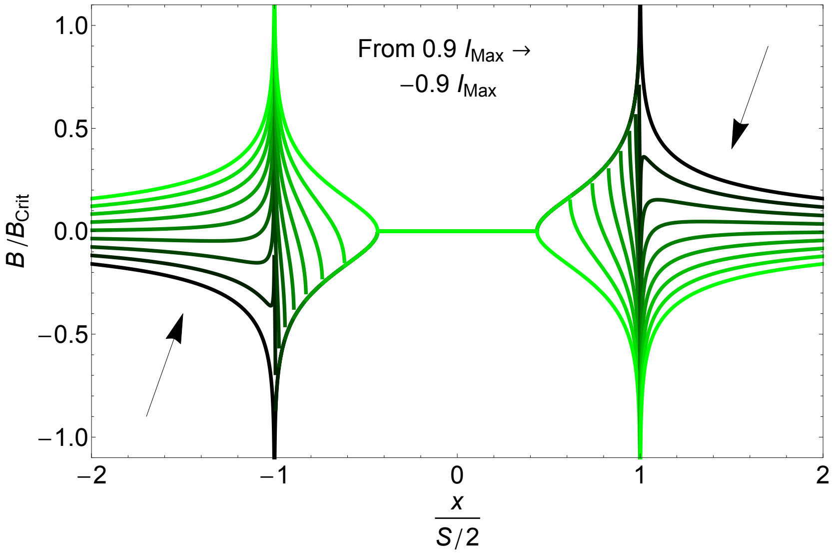

Figure 17: Magnetic field hysteresis due to a transport current in the superconducting strip that is gradually being lowered. The current stepwise decreased from $0.9{\cdot}I_{Max}$ to $-0.9 \cdot I_{Max}$. Note that the x-axis of the figure ranges further than just the width of the strip.

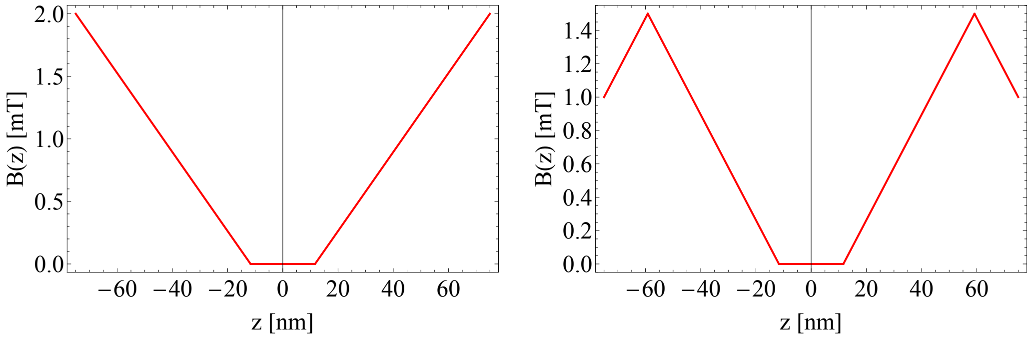

(a) An external field of 2 mT was applied to the virgin strip.

(b) First, a field of 2 mT was applied and then reduced to 1 mT.

Figure 18: Magnetic field penetrating the superconductor according to the Bean model. Note that the figures do not show a cut along the x-direction of Figure 8 but along the z-direction.

where B_{Bean} is again given by Equation 54. This behavior is shown in Figure 18a. If we rise the external field above B_{Bean}, the superconductor will be fully penetrated by field because the currents are not strong enough to shield the center region from the external field.

The hysteresis $B^{\downarrow}_{In}(z, B_a, B_{Max})$ that occurs upon changing the applied field is shown in Figure 18b. It can be expressed as

$$B^{\downarrow}_{In}(z, B_a, B_{Max}) = B_{In}(z, B_{Max}) - 2 \cdot B_{In}\left(z, \frac{B_{Max} - B_a}{2}\right). \tag{65}$$

The NBI Field Model due to an External Magnetic Field Brandt and Indenbom also calculated the magnetic field in a superconducting strip in an externally applied magnetic field B_a [30]. We use again the geometry in Figure 8, where the field is perpendicular to the strip surface. The expression for the magnetic field in and around the resonator is given as

$$B_{In}(x, B_a) = \begin{cases} 0, & |x| < b(B_a), \\ B_{Crit} \operatorname{arctanh}\left(\frac{\sqrt{x^2 - b^2(B_a)}}{C(B_a)|x|}\right), & b(B_a) < |x| < \frac{S}{2}, \\ B_{Crit} \operatorname{arctanh}\left(\frac{C(B_a)|x|}{\sqrt{x^2 - b^2(B_a)}}\right), & |x| > \frac{S}{2}, \end{cases} \tag{66}$$

where the functions $C(B_a)$ and $b(B_a)$ are given by Equations 57 and 58. The critical field for this model, B_{Crit}, is given by Equation 59 as 9.5 mT. Figure 19 shows the field in and around the superconducting strip for various

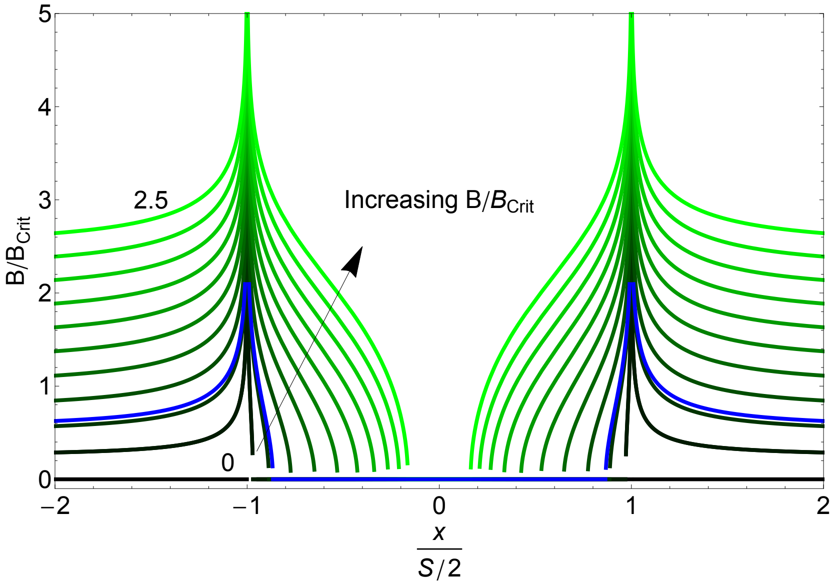

Figure 19: Magnetic field in the vicinity of the superconducting strip due to an externally applied magnetic field. Note that the x-scale covers more than just the strip.

external fields. The blue line is the field distribution due to a perpendicular external field of strength $B_a = \sin(1°) \cdot 0.3\,\mathrm{T}$=5.2 mT. Again, at the edges of the strip appear logarithmic singularities. The magnetic field in this model has a stronger drop off compared to the model with the transport current. In the former model, the magnetic field penetrates quite far into the strip although its value is rather small. In this model, this seems not to be the case.

The hysteresis $B^{\downarrow}(x, B_a, B_{Max})$ of this curve is given as

$$B^{\downarrow}(x, B, B_{Max}) = B_{In}(x, B_{Max}) - 2 \cdot B_{In}\left(x, \frac{B_{Max} - B_a}{2}\right) \tag{67}$$

with $B_{In}(x, B_a)$ given in Equation 66. This is shown in Figure 20 where it is apparent that upon reducing the initial field the strongest changes happen close to the edge of the superconducting strip. Also, it should be noted that the total field strength is by far strongest close to the edges of the strip.

4.7 Comments on the Different Dissipation Models

It is important to think again about which kind of dissipation is measurable. As we essentially measure the quality factor of the resonator, the measurement is only sensitive in losses of the resonating current density. This is the

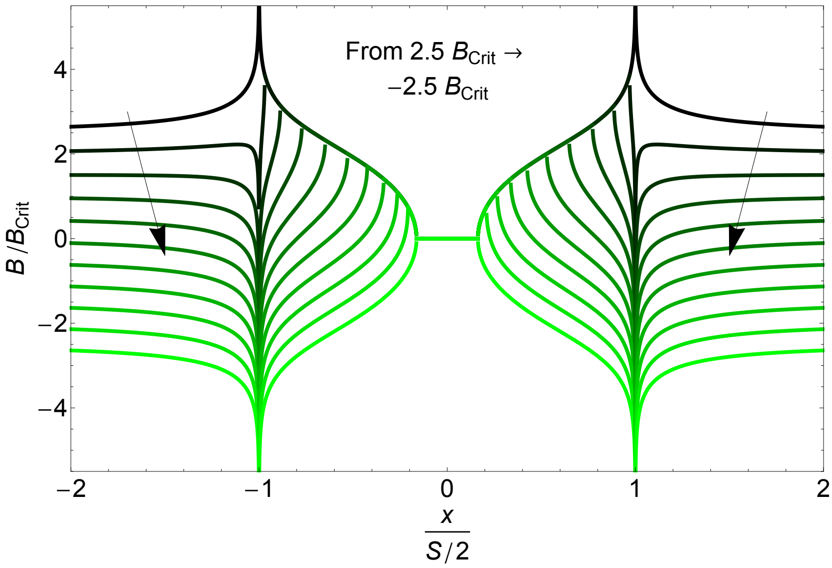

Figure 20: Hysteresis in the magnetic field in a superconducting resonator that appears due to an initially applied field $B_{Max} = 2.5\,B_{Crit}$ that is gradually lowered to $-2.5\,B_{Crit}$.

current density that comes due to a transport current. Therefore, losses due to the shielding current in the superconductor are not measured with this method. There is also dissipation due to shielding currents, but the power needed for the dissipation is provided by the magnetic field. Hence, not all the presented current models are suitable candidates to be put into Equation 30. Only the constant current density, the LW model and the current density due to a transport current by NBI come into consideration. The two models by Bean and NBI that describe the density of the current induced by an external field are not suitable.

For the magnetic field models, we can only rule out one from physical reasons. It is the model by NBI that describes the magnetic field in the resonator that is due to a transport current. This is not depending on an externally applied field, and can therefore be accounted for in the constant contribution $\Delta E_{tot,0}$ in Equation 35.

The model combinations using the constant current density both do not reflect the behavior of the data obtained. Also, the value for the losses the combination of the constant current model and the NBI-field due to an external field is a factor 50 too low. The value obtained from the combination of the constant current density and the Bean field is a factor 20 too low. Therefore, we will not consider these two model combinations any further.

Similarly, we can rule out the Bean model for the description of the field inside the resonator. The combination with the LW current model yields losses that are a factor of 35 too high. The combination with the NBI current distribution due to a transport current yields a value that is a factor of 85 too high. Also, the shape of the curves obtained does not match with the measured data.

Therefore, we can conclude that we need to consider only two models. These are the ones combining the field in the resonator due to an external field with the current densities due to a transport current and the approximation of a flux free current distribution by Lahl and Woördenweber.

5 Measurement Setup and Data Acquisition

Here, we shall have a look at how the measurements are done and what the microwave setup is. A typical measurement curve is analyzed and it is discussed how a typical hysteresis measurement is performed. Also, a description of the samples used is given.

5.1 Microwave setup

The quantity we measure is the transmission through the resonator, depending on frequency and magnetic field (compare Section 4.2). The transmission function is a Lorentzian, compare Equation 31. We will sweep the frequency of the signal sent to the resonator and measure the transmission for one configuration of parameters (magnetic field, angle). Then, we fit Equation 31 to the obtained data, extract resonance frequency f_{Res} and peak width Δf from the fit and calculate the quality factor, Equation 32.

The FPGA we use to acquire the signal has a bandwidth of 250 MHz. As we are using frequencies in the order of 2 GHz, a heterodyne detection scheme [33] is used to down convert the microwave signal. This is done by a mixer with the help of the local oscillator signal that is 250 MHz lower than the signal we want to study, for details see Ref. [33].

A schematic of the microwave electronics is shown in Figure 21. It is comparable to microwave setups used in this lab before [34, 35]. One of the challenges is shielding the sample from room temperature thermal photons. This can be achieved by placing an attenuator on the cold stage of the fridge. Another important point is to get a good signal to noise ratio, which can be obtained by placing filters, attenuators and amplifiers in a meaningful way. Also, one should be aware of standing waves that can appear between circuit elements. These can be suppressed by placing attenuators between circuit elements. To to a temporary lack of 3 dB attenuators, some 10 dB attenuators

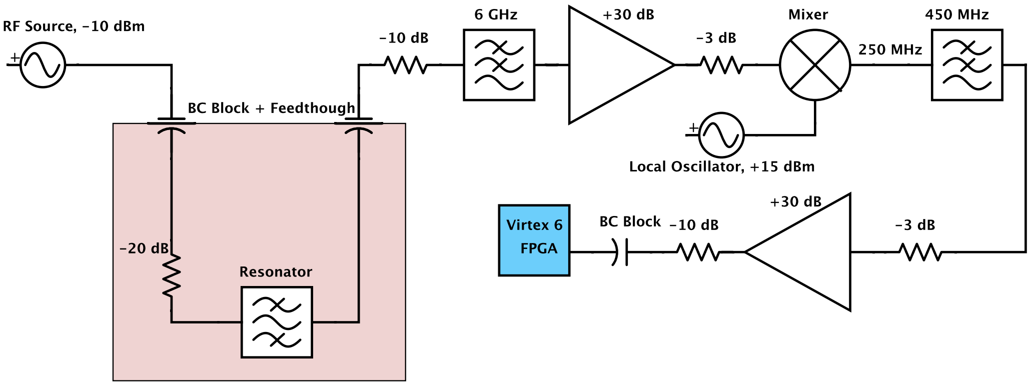

Figure 21: A schematic of the microwave setup used. The red box indicates the fridge. A detailed description can be found in the text.

had to be used. At the moment, there is no cold attenuator in the setup, but this would be the next thing to implement.

The signal is sent through the sample, it is amplified at room temperature and then down converted to 250 MHz. After the down conversion, it is again amplified and sent to the FPGA which performs the data acquisition. The data is sent per LAN to the measurement computer.

5.2 Analysis of a Frequency Sweep

The recorded data are transmissions spectra. A typical curve is shown in Figure 22a where the blue points indicate the measured data. The red line is the fit to these points. The model for the fit is given by Equation 31. The fitting procedure is done in Mathematica. A least mean square method is used to optimize the fit. Figure 22b which uses the same units as Figure 22a shows the difference between the raw data and the fit. The maximal deviations are a bit less than one tenth of the value. Also, it can be seen that the data indicates a slightly asymmetric Lorentzian curve (the deviations on left hand side of the peak are positive, whereas the deviations on the right hand side tend to be negative). It would therefore be possible to account for this asymmetry by using another fit model. However, for our purposes it is useful to get fast fits, and the error made was sufficiently low to leave a more involved model on the side.

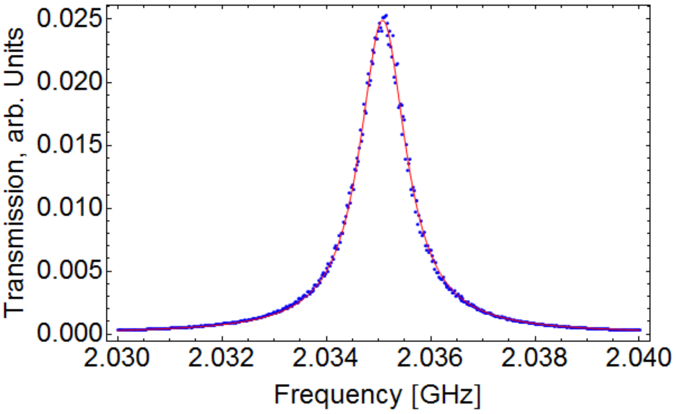

(a) The raw data is shown as blue points. The fit is shown as a red line.

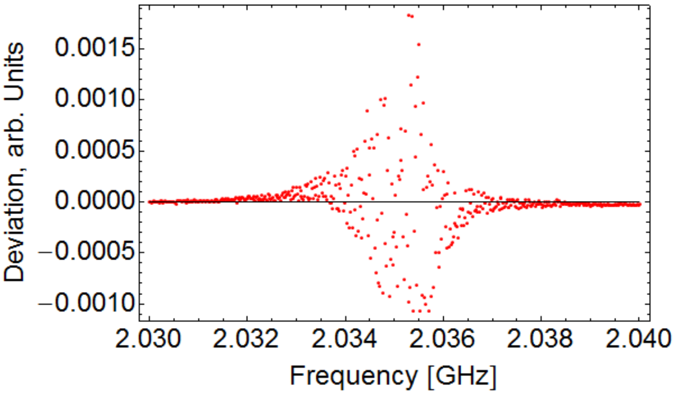

(b) The deviation of the data from the fit. The difference between data and fit is plotted.

Figure 22: Analysis of the data obtained by the FPGA. What is used later on are the parameters from the Lorentzian fit, Equation 31.

5.3 Samples

The coplanar wave guide resonators we use to perform the experiments do not for all the experiments have the same properties. Various groups and different experiments have shown that placing holes in the center conductor and the adjacent ground can reduce the losses in a coplanar waveguide resonator [19, 20, 36–40]. If the pinning potential of the vortices has a clear minimum at a well defined place, the vortices will not move too far out of it. For example, one could approximate the pinning sites as harmonic potentials, which then limits the movement of the vortices. We will account for this effect by adjusting the vortex viscosity η in Equation 30.

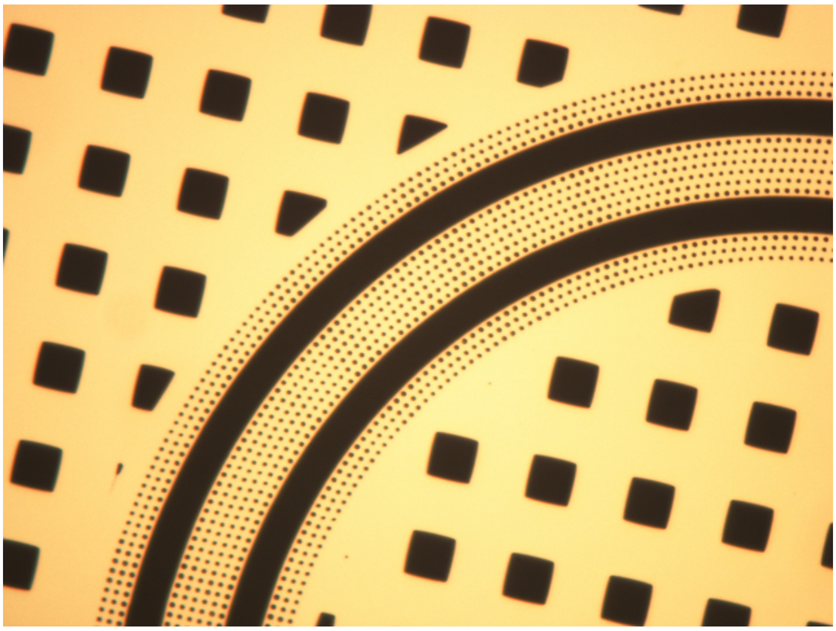

Figure 23: A zoom-in on a coplanar waveguide resonator with holes in the center conductor to trap vortices. The large holes in the ground planes serve the same purpose. Image by courtesy of M. Allan.

The physical properties of the resonators used are summarized in Appendix B. There, material properties, geometry parameters chosen by the designer and the resonator parameters are listed.

A resonator that has holes in the center conductor is shown in Figure 23. The sample fabrication shall not be discussed here, as the author was not involved in this process.

We will discuss in the coming sections that these holes indeed do help to reduce the losses due to vortices. For this purpose, we will measure the losses of resonators with and without holes in the center conductor.

5.4 Hysteresis Measurements

We use two different devices to make a cold surrounding for the measurement. On the one hand, this is the Arcitc, for which the sample holder was constructed. On the other hand, we also use a dipstick, that can be dunked into liquid helium. Using a dipstick allows you to cool down a sample very quickly, which gives an obvious advantage compared to the Arctic, which has a cool down time of some 12 hours. The disadvantage however is that the cold temperature is just liquid helium temperature, 4.2 K. The dipstick was made by Milan Allan, and there are two coils mounted on it. The coils are made out of the same wire as it is used for the coils I designed. The coils have less windings, but are closer together. They can hold a current of 300 mA and source a magnetic field of 170 mT in the sample region. They probably can hold such a high current because the cooling due to the surrounding liquid helium is much better than in the Arctic. The field is parallel to the surface, but it is hard to measure how well the alignment between coils and sample is.

The hysteresis curves we will discuss in the following are obtained by sweeping over two parameters. The slow parameter is the magnetic field, the fast parameter is the frequency. Underlying to each point in these curves is a Lorentzian as in Figure 22 that measures the frequency dependent transmission for a given value of the applied magnetic field. The fit to this Lorentzian then yields the parameters that determine the point of the curve.

When measuring hysteresis curves, the applied magnetic field is usually 0 in the beginning, then ramped up to a certain value B_{Max}. After that, the field is ramped down to the negative of this value, $-B_{Max}$, and again ramped up to B_{Max}. The course of the magnetic field is relevant, as indicated by the coloring. The color of the points changes, starting from black and getting more and more red. Subsequent points are connected with a blue line in the hysteresis plots. A typical data set is displayed in Figure 24 where arrows indicate the direction of the magnetic field sweep.

The change in the quality factor respectively the losses is not only due to a change in the peak width, but also due to a change in the resonance frequency. Although one does naively not expect a change in the resonance frequency upon application of a magnetic field. And the changes are indeed very small, compare Figure 25. However, they can be explained by a change in kinetic inductance ΔL_K of the resonator. The kinetic inductance is an effect due to the mass of the charge carriers. A change in the electric field will be opposed due to the inertia of the charge carriers. This yields an effective inductance. This effect only appears in samples with high carrier mobilities and at high frequencies. As the present case is a superconductor, the high mobility of the carriers is provided, and gigahertz frequencies are sufficient to observe kinetic inductance. The kinetic inductance is given as

$$L_K = \left(\frac{m}{2n_S e^2}\right)\left(\frac{l}{A}\right) \tag{68}$$

where m is the electron mass, n_S the Cooper pair density, l the resonator length and A its cross section. A change in the kinetic inductance can be expected, as the Cooper pair density is is dependent on the magnetic field. Using $\Delta f_{Res} = 1/2\pi\sqrt{LC}$, the data for f_{Res} in Figure 25, the usual geometry

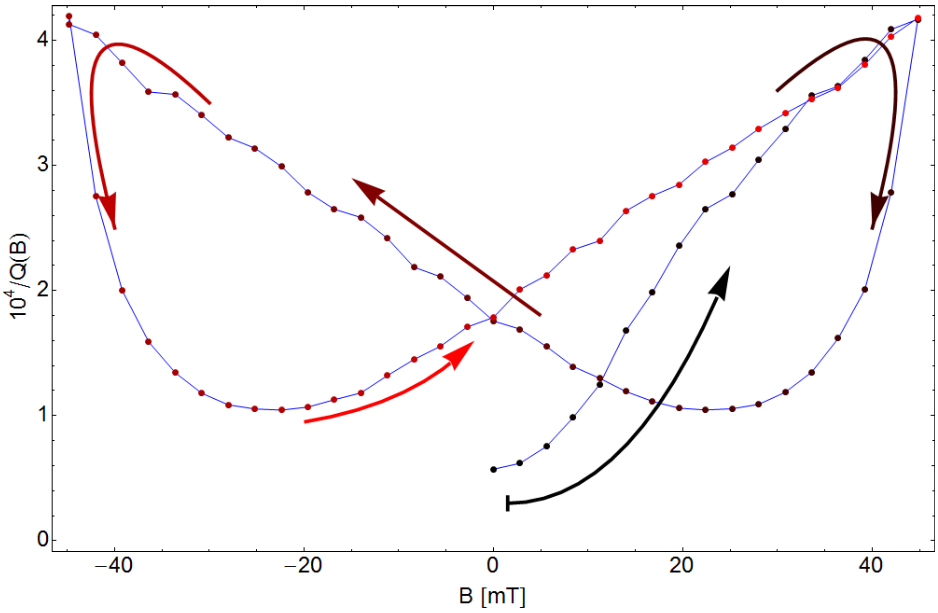

Figure 24: A typical hysteresis curve. The reverse of the quality factor $1/Q(B)$ is displayed. The magnetic field is swept from 0 to 45 mT, then to -45 mT and up to 45 mT again. Arrows indicate the sweep direction, the coloring of subsequent points changes from black to red.

parameters and the $L = 2.5\,\mathrm{nH}$ given in equation 42 one can estimate $\Delta n_S \approx 5 \cdot 10^{27}\,\mathrm{m}^{-3}$. This number can be compared to a typical electron density of some $10^{29}\,\mathrm{m}^{-3}$ in a metal. Therefore, the change in kinetic inductance is a plausible explanation for the change in the resonance frequency of the resonator.

6 Dipstick Measurements

In this section, we look at different hysteresis measurements performed at liquid helium temperature. We will compare resonators that have no holes in their center conductor with resonators that have holes. The data for high fields will be explained quantitatively with the model for the losses derived in section 4. We will see that for lower fields, this model is not able to explain the data obtained.

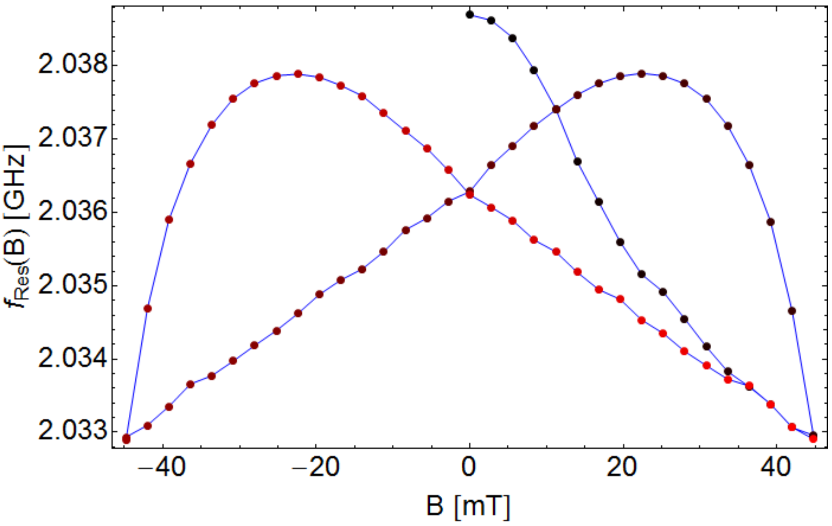

Figure 25: The typical hysteretic behavior of the resonance frequency as the magnetic field is swept. The resonance frequency is plotted in GHz against the magnetic field in mT. For clarity, the arrows as in Figure 24 are left away.

6.1 Low Field Hysteresis Measurements

Now we will discuss the hysteresis curve of a resonator without holes measured with a dipstick. The applied currents correspond to a field of $\approx 45\,\mathrm{mT}$. The data obtained are shown in Figure 26. These are the resonance frequency and the peak width of the transmission spectrum. From this, we can deduce the field dependent quality factor and the losses, see Figure 27. The ordering of the points in both Figures is again the same as in Figure 24, but the arrows are omitted for better readability. All the plots have the same x-axis that corresponds to the applied magnetic field.

Figure 26a shows the change in the resonance frequency as a function of the magnetic field. One can observe that the changes are small. The change in the peak width of the resonator, shown in Figure 26b, changes by a factor of four during the up and down sweeps. Therefore, the changes in the quality factor, Figure 27a are dominated by the changes in the peak width.

Now we will focus on fitting the $1/Q(B)$ data. After presenting different models for the current distribution and magnetic field distribution in the resonator in sections 4.5 and 4.6 and the subsequent discussion in section 4.7 we are left with two models.

The downside of these models is their calculation time as they are highly nonlinear. This is because each point in the model is obtained by an integration over a strongly peaked function that seems not to have an analytical

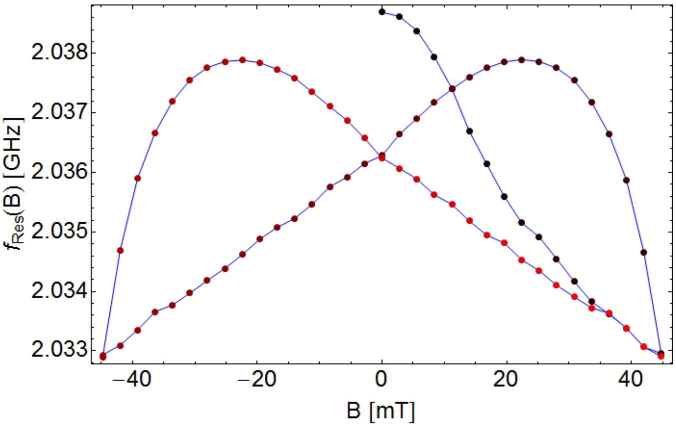

(a) Hysteresis of the resonance frequency in GHz.

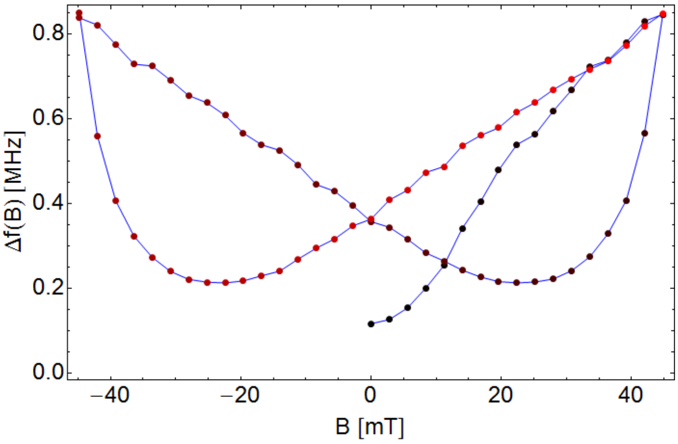

(b) Hysteresis of the peak width in MHz.

Figure 26: The hysteresis of the frequency and the peak width dependent on the applied magnetic field in mT.

solution. Therefore, a numerical Monte Carlo integration procedure is necessary. Several tricks to reduce the computation time are used, like integrating only over half of the strip and doubling the result or mirroring the down sweep function at $B = 0$ to get the function for the sweep from $-B_{Max}$ to B_{Max}. To get an order of magnitude estimation, the models were first evaluated at only some 25 points. Only in the end, the values obtained from these estimations could serve as starting values for a fitting routine that minimizes the error squares. Depending on the model, a fitting routine can take several days to converge.

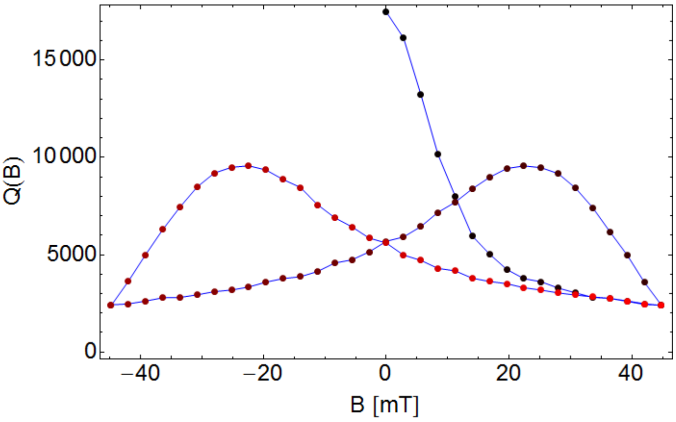

(a) Hysteresis of the quality factor.

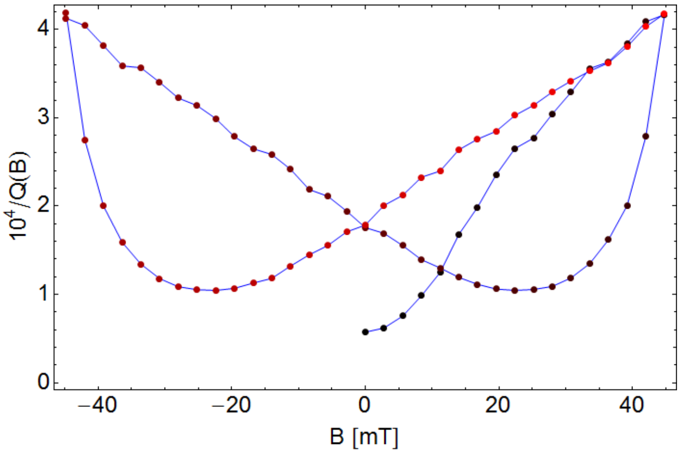

(b) Hysteresis of the total losses times 10^4.

Figure 27: The hysteresis of the quality factor and the total losses dependent on the magnetic field in mT.

The LW model In Figure 28, the hysteresis from Figure 27b is shown. The field range is 45 mT. The green curve is an approximation of the model to the data. The approximation is not a least mean square fit, but it is done just by eyeball. This is because the proper fitting procedure takes several days. The model used is given as Equation 35 when Equations 30, 36, 46, 66 and 67 for P_{Stored}, $j(x,z)$ and $B^{(\downarrow)}(x,z)$ are used. For the applied magnetic field it is important that only the perpendicular component is taken into account. If α is the angle between the plane and the applied field, the perpendicular component of the magnetic field is $B_\perp = \sin(\alpha)B$. This yields the fit equation

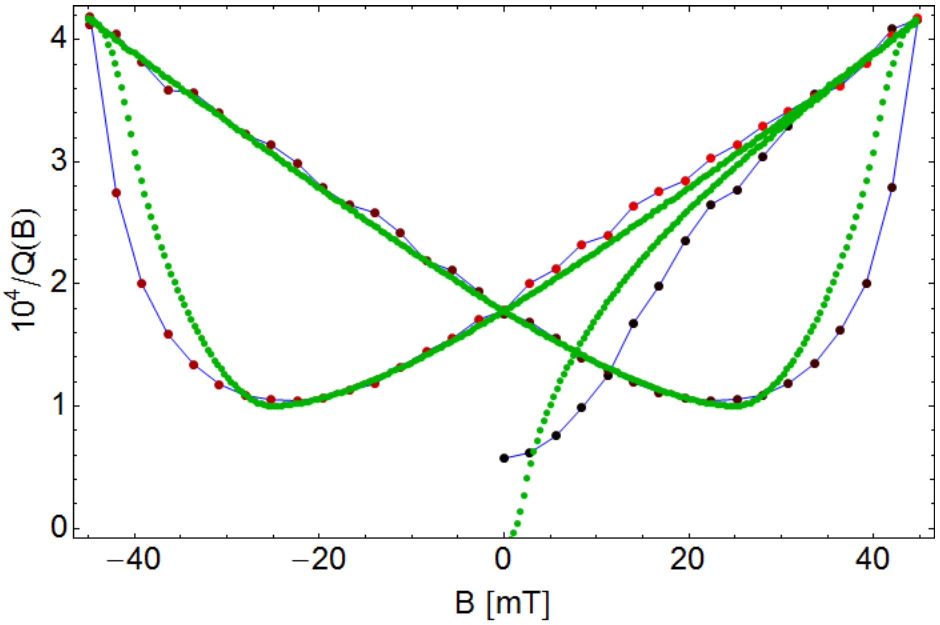

Figure 28: Magnetic field hysteresis. $1/Q(B)$ is plotted against the magnetic field. The black-red points are measured data, the green points are a fit using the LW current distribution in a resonator and the NBI field due to an external field.

for the LW current density model,

$$\frac{1}{Q(B)} = \frac{\Delta E_{tot,0} f_{Res}}{2\pi P_{Stored}} + \frac{\Phi_0 f_{Res} l \cdot d}{8\pi\eta P_{Stored}\cdot\gamma} \cdot \\ \cdot \int_{-S/2}^{S/2} j^2(x, I_a, \lambda_L) \cdot |\sin(\alpha) B^{(\downarrow)}(x, B_{Crit})| \mathrm{d}x. \qquad (69)$$

The arrows in brackets on the magnetic field indicate that depending on the history of the magnetic field the appropriate functions have to be chosen. The parameter γ is of order of unity and should account for deviations in the vortex viscosity η and the total inductance L of the resonator.

The parameters used in the fitting curve are listed in the following table.

Critical current	j_{Crit}	$3.2 \cdot 10^9$ A/m^2
Angle	α	0.5 °
London penetration depth	λ_L	30 nm
Multiplication factor	γ	2.5
Zero field losses	$1/Q(0)$	$-1.4 \cdot 10^{-5}$

Some of the parameters used for the fit have somewhat questionable values. The critical current density is a factor five lower than expected. But considering the wide spread of the values mentioned by the different sources in section 4.4 this still could be possible. Also the losses at zero field are assumed to be negative such that the curve fits better. This is clearly not physical. But the parameters for the London penetration depth, the angle between field and sample and the multiplication factor seem to be in a reasonable range.

Note that the dependence on the transport current in the resonator I_a is not important, as in the second part of Equation 69 it cancels out. There is both an I_a^2 from the $j^2(x, I_a, \lambda)$ in the nominator and an I_a^2 from P_{Stored} in the denominator. The I_a^{-2} dependence in the first term can be accounted for with $\Delta E_{tot,0}$.

We can see that the data obtained by ramping the field up to 45 mT from the virgin state is not well fitted. The behavior of the fit curve is different, and also the losses at zero field are not predicted properly. However, the down sweep curve is fitted quite nicely, and its characteristics are displayed well.

The NBI model We can also use the NBI model to fit the data. This is obtained by inserting Equations 30, 36, 48 respectively 51 and 66 respectively 67 in Equation 35. Therefore, the fit Equation for the NBI current density model is

$$\begin{aligned}\frac{1}{Q(B)} =& \frac{\Delta E_{tot,0} f_{Res}}{2\pi P_{Stored}} + \frac{\Phi_0 f_{Res} l \cdot d}{8\pi\eta P_{Stored} \cdot \gamma} \cdot \\ & \cdot \int\limits_{-S/2}^{S/2} j^{(\downarrow)\,2}(x, I, j_{Crit}) \cdot |\sin(\alpha) B^{(\downarrow)}(x, B_{Crit})| \mathrm{d}x, \qquad (70)\end{aligned}$$

where l is the length of the resonator and L denotes the resonators total inductance and appears in the definition of P_{Stored}. Again, the arrows in brackets on the field and the current density indicate that depending on the history of the magnetic field the appropriate functions have to be chosen and also γ is the same as before.

Figure 29 shows a fitting curve using the NBI current density model. The fit is again made by eyeball, and does not minimize error squares. The parameters used in the fitting procedure are listed in the following table.

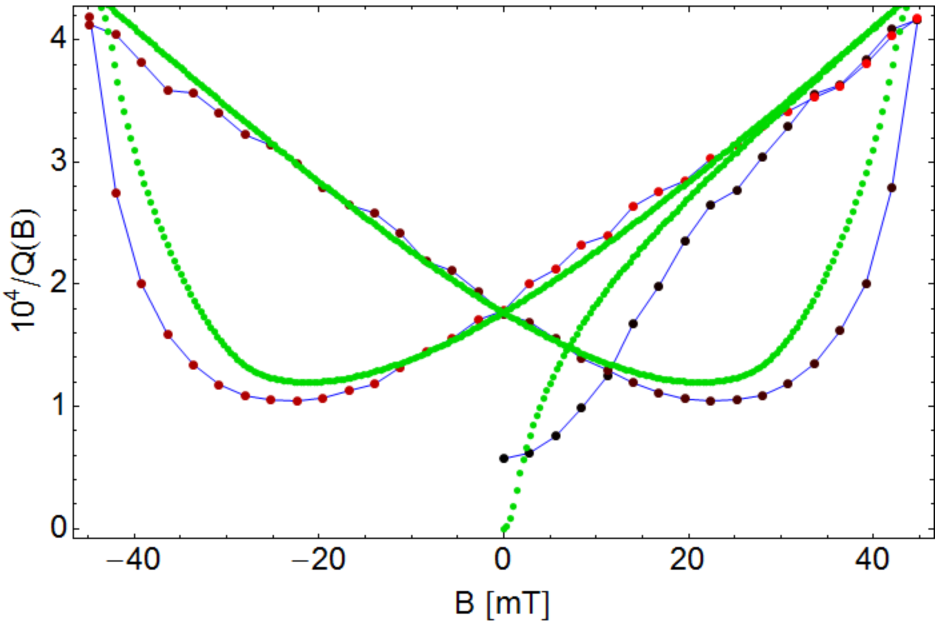

Figure 29: Magnetic field hysteresis. $1/Q(B)$ is plotted against the magnetic field. The black-red points are measured data, the green points are a fit using the NBI current distribution in a resonator due to a transport current and the NBI field due to an external field.

Transport current	I_a	0.4 mA
Critical current	j_{Crit}	$4.8 \cdot 10^9\ \mathrm{A/m^2}$
Angle	α	1 °
Multiplication factor	γ	9
Zero field losses	$1/Q(0)$	0

The transport current in the resonator is an order of magnitude lower than expected. This can still be physical, as the estimation in section 4.3 is rather crude. The critical current density is also rather on the low end. Both, the multiplication factor and the angle are surprisingly high. The zero field losses are assumed to be zero such that the curve fits nicely. This can of course not be true. All these parameters are quite a bit off of what we would expect for them. However, a proper fit that minimizes the error squares would be required to make precise statements about them.

At this point it should be emphasized that it was not clear from the beginning that this data could be explained with the models used. For example D. Bothner et. al. in Ref. [20] state that "[this] theoretical model is too simple to be used for a quantitative analysis of our experimental data".

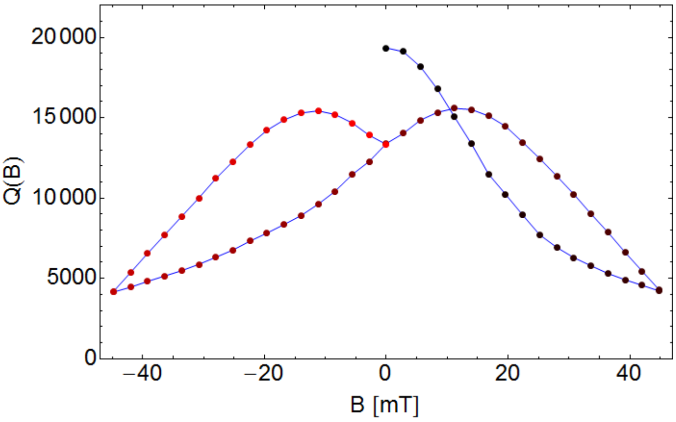

(a) Hysteresis of the quality factor.

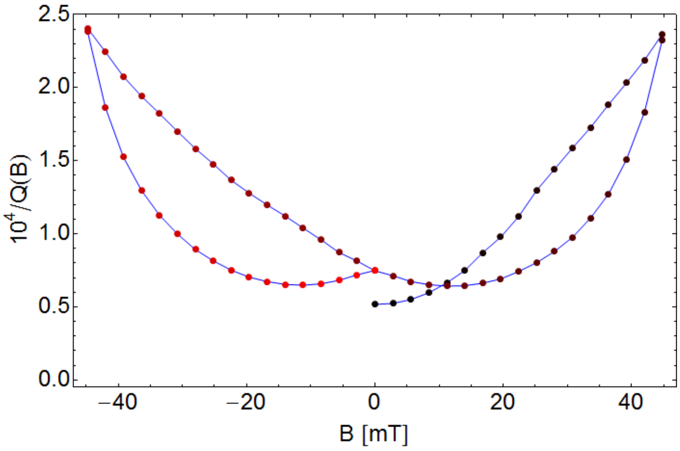

(b) Hysteresis of the total losses times 10^4.

Figure 30: The hysteresis of the quality factor and the total losses dependent on the magnetic field in mT. The measurement was performed using a dipstick. The sample is a resonator that has holes in the center conductor, as shown in Figure 23.

Holes in the center conductor Now, we want to compare a resonator with no holes as discussed above with a resonator that has holes. This will allow us to see that the holes in the center conductor indeed help to reduce the losses. Figure 30 shows the quality factor and the total losses of a resonator with holes. Except for the holes, the geometrical properties are chosen to be the same as for the resonator used before. The up-sweep from -45 mT is not performed to +45 mT, but just until zero field.

Figure 31 shows the curves from Figures 27b (no holes, depicted in red) and 30b (with holes, depicted in green) in one plot. It is clearly visible

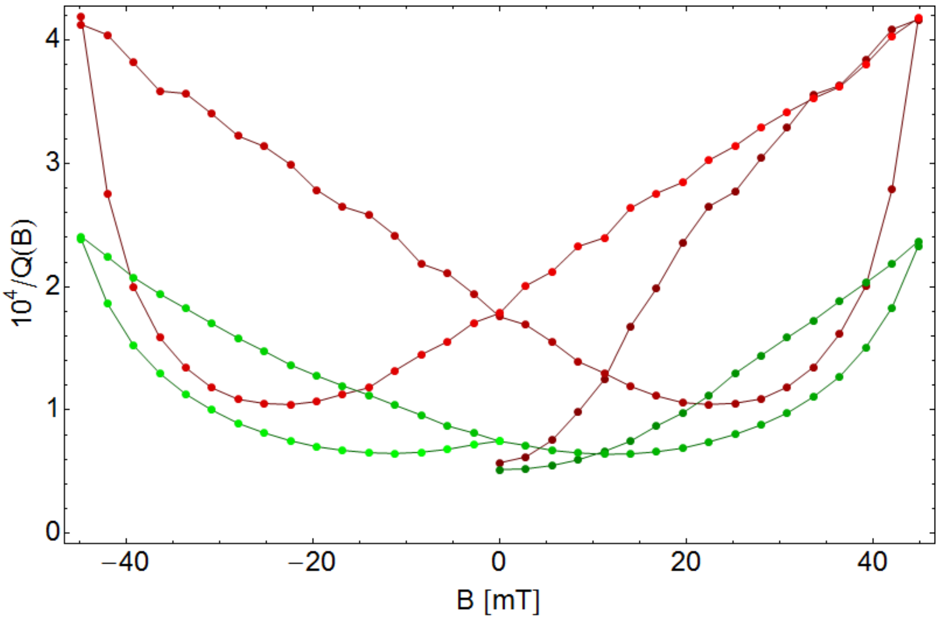

Figure 31: The losses of resonators without (red curve) and with (green curve) holes. Plotted are the data from Figures 27b and 30b.

that the losses in the resonator without holes are 1.6 times higher than in the resonator that has holes. There is also a difference in the shape of the curves. The resonator without holes has a fast decrease in losses as the field is lowered from an extreme value. After the losses reach a minimal value, they increase almost linearly with increasing field. This is not the case for the resonator with holes. There, the losses decrease a lot slower after an extreme value. The minimum is at a field closer to zero, and after passing the minimum, the increase in losses is not linear but seems to be quadratic. Therefore, one can clearly say that it is favorable to have holes in the center conductor of the resonator as magnetic fields are applied. It reduces the losses and also the hysteresis is lower.

6.2 High Field Hysteresis Measurements

As the coils of the dipstick are plunged in liquid helium, the cooling power acting on the coils is very high. This allows for relatively large currents in the superconducting wires - remember the onset of resistance in these wires at high currents, as discussed in Ref. [12]. Hence, the applied fields can go up to 160 mT. A hysteresis curve with this field was measured, as shown in Figure 32. The sample is a niobium resonator with a center conductor that has holes in it. At the high field ends of the plot, the losses do not increase any further.

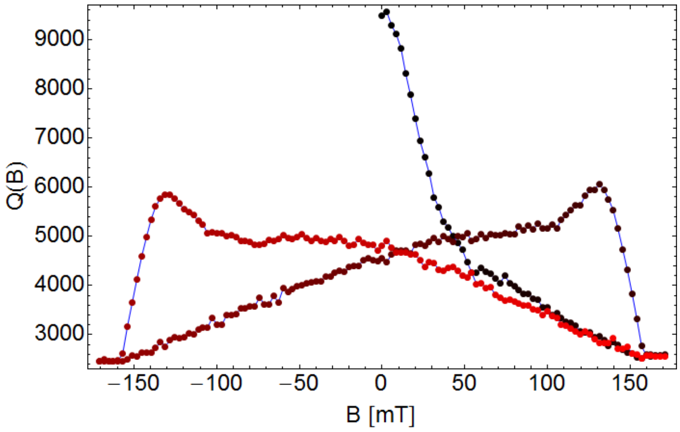

(a) The behavior of the quality factor upon sweeping the magnetic field.

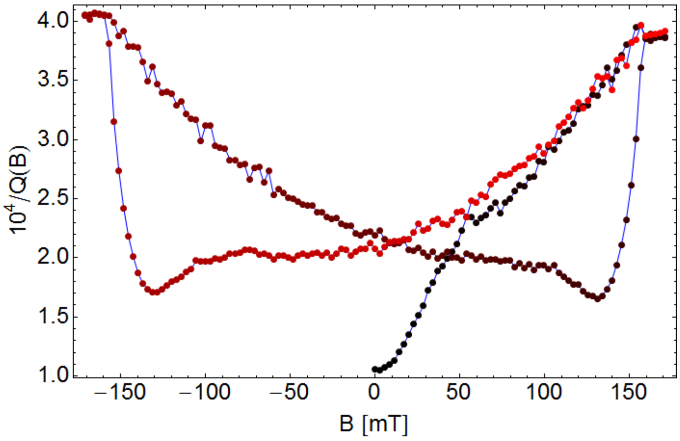

(b) The total losses times 10^4 upon sweeping the magnetic field.

Figure 32: The magnetic field is plotted in mT. Starting from zero field, it is swept between ±170 mT. The measurement is performed using a dipstick and a resonator with holes in the center conductor. Note that the maximal field actually sourced is only 160 mT, compare text.

This has the profane reason that the current source used to power the coils went in a limit that restricted the maximally sourced current. Therefore, the data points above a field value of 160 mT do not really correspond to the field strengths indicated in the plot.

Careful observation of the data reveals a new feature compared to the data discussed so far. As the virgin state is swept up, the losses first increase considerably, and then seem to increase with another slope starting from a

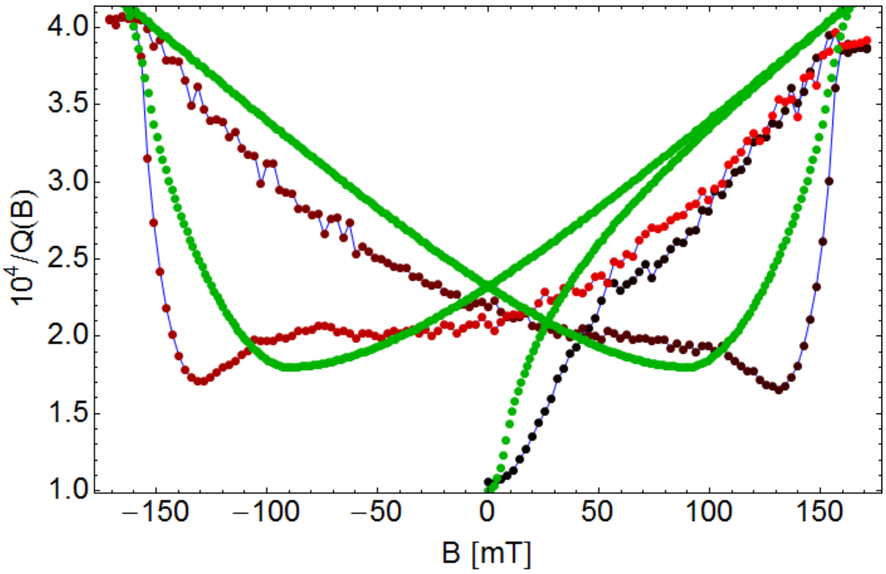

Figure 33: The data displayed in Figure 32b is roughly fitted (green curve). The fit is obtained using Equation 69. The fit captures some essential characteristics of the data, but not all of them.

field of 55 mT. On the down sweep, a very sharp decrease in the losses can be observed. After a slight increase, the losses stay almost constant until the field is at 0 again. Then, the losses increase and follow quite nicely a parabolic law.

We can again apply the models given in Equations 69 and 70. The first model, with the approximation of the flux free current density in a resonator, is fitted to the data and shown in Figure 33. The green curve shown is not a least squares fit, but just obtained by adjusting the parameters by eyeball. This is because a fitting procedure for this curve takes several days to be evaluated on an ordinary computer. The fit is just evaluated at several points because letting Mathematica plot such a curve takes a lot of time. The most essential features of the data are captured, however many details are still missing. First, the virgin up-sweep curve shows a different shape, its second derivative is negative instead compared to the positive second derivative of the data. Although, the first few points in the fit also have a positive second derivative. Then, the strong decrease after the field extreme is not captured enough by the model. Also, the subsequent increase in losses to the next extreme follows rather a linear behavior than a quadratic.

However, the model still seems to give a reasonable quantitative description of the data. The parameters used for the fit are listed in the following table.

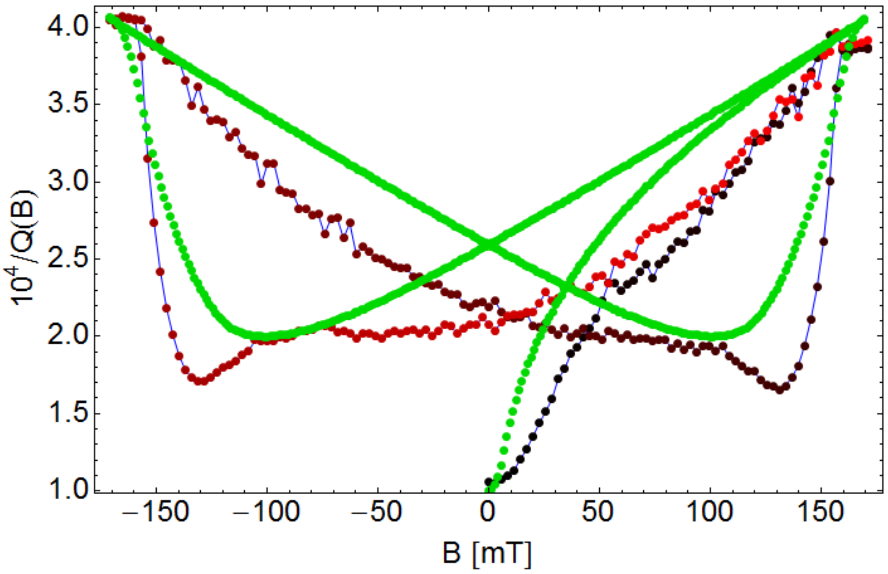

Figure 34: The data displayed in Figure 32b is roughly fitted (light green curve). The fit is obtained using Equation 70. The fit captures some essential characteristics of the data, but not all of them.

Critical current	j_{Crit}	$4 \cdot 10^9\,\mathrm{A/m^2}$
Angle	α	$0.2\,°$
London penetration depth	λ_L	$37\,\mathrm{nm}$
Multiplication factor	γ	4.5
Zero field losses	$1/Q(0)$	10^{-4}

The angle and the London penetration depth are as one would expect. But both, the critical current density and the multiplication factor that accounts for deviations in the critical magnetic field and the normal state resistivity are considerably off the expected values.

We can also use the NBI transport current model to make a fit to the data shown in Figure 32b. Again, due to a big computational effort to make a least square fit, only a eyeball fit evaluated at several points is presented in Figure 34. This fit also covers the essential features of the data, but is missing some details. Again, the virgin up-sweep in the fit is too steep, and the turning point in the slope does not coincide with its analog in the data. But this fit has a stronger decrease in the losses right after the extrema of the field. Another difference is that the increase in the losses towards the next extrema seems to be more linear than in the previously discussed fit. The parameters used for this fit are listed in the following table.

Transport current	I_a	$0.5\,\mathrm{mA}$
Critical current	j_{Crit}	$9.6 \cdot 10^9\,\mathrm{A/m^2}$
Angle	α	$0.25\,^\circ$
Multiplication factor	γ	20
Zero field losses	$1/Q(0)$	10^{-4}

Here, the critical current and the angle are in a range that can be expected. But the transport current is a factor 6 lower than estimated in section 4.3, which is quite a big deviation. The multiplication factor γ is 20. This makes the model rather unreliable, as such a high deviation is not expected. It seems that to fit this data another model for the magnetic field might be required to capture further details in the data.

The change in the slope of the virgin up-sweep could be related to a change of the underlying physics. There are some 36 holes in the center conductor of the resonator per $10\,\mu$m resonator length, compare Figure 23. The vortices are trapped in these holes. If the field is deviated by 0.5° and has a strength of 55 mT, the number N of vortices in the same area is approximately given by

$$N = \frac{\sin(0.5^\circ)B}{\Phi_0}A = 2.4 \cdot 10^{11}\,\mathrm{m}^{-2} \cdot (10\,\mu\mathrm{m})^2 \approx 24.$$

This means that each hole in the resonator is occupied with a vortex. If new vortices try to enter the center conductor, they will need more energy for this process than the previous vortices. This is because they can not enter an empty hole due to vortex-vortex repulsion. Therefore, the increase in vortices in the center conductor is hampered in this situation. As there are fewer vortices entering the superconductor, also the dissipation due to vortices will not increase as fast before. This hand-waving argument would also explain the smaller slope of the increase in losses after the turning point at 55 mT.

6.3 Alternating Raise

We thought that it might be instructive to increase the applied magnetic field in an alternating way. This means, that the field is first zero, then increased to 5 mT, decreased to -5 mT, increased again to +10 mT and so on. A rise in the magnetic field like this could give some information about the hysteresis. For this experiment, a resonator without holes is used, and the measurement was performed with the dipstick.The result of the measurement is shown in Figure 35. Again the same color coding as before is used, although the readability clearly reaches a limit here, especially for the low field values. An interesting feature is that the losses at a given field strength, for example

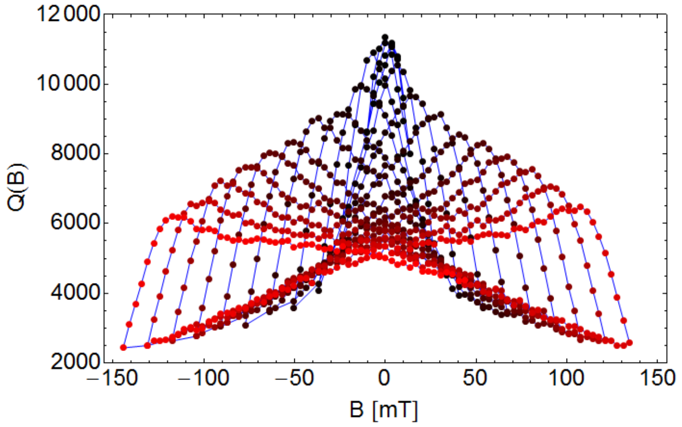

(a) The behavior of the quality factor upon an alternating rise of the magnetic field.

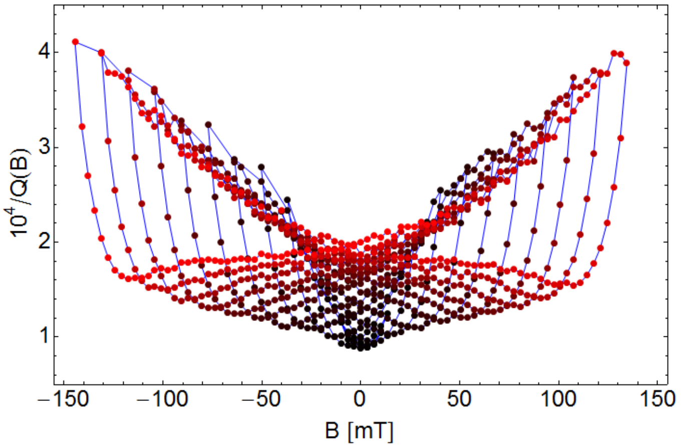

(b) The total losses times 10^4 upon an alternating rise of the magnetic field.

Figure 35: The magnetic field, plotted in mT, is raised in an alternating way. The plotted curves are the quality factor and the total losses.

at 75 mT in Figure 35b, are lower the extremer the previous maximal value was. In the figure, this can be seen as the more red the points are, the less losses they have in the up sweep curve at a field value of 75 mT. This can be understood that the previous extreme value is still damping the losses in the resonator. This is because the magnetic field in the resonator still is dependent on the most recent maximum, compare Figure 20.

To get a better understanding of what is happening at low fields, Figure 36 only shows the first few steps until the field reaches maximal values that exceed 50 mT. Observing the points between two consecutive extreme values,

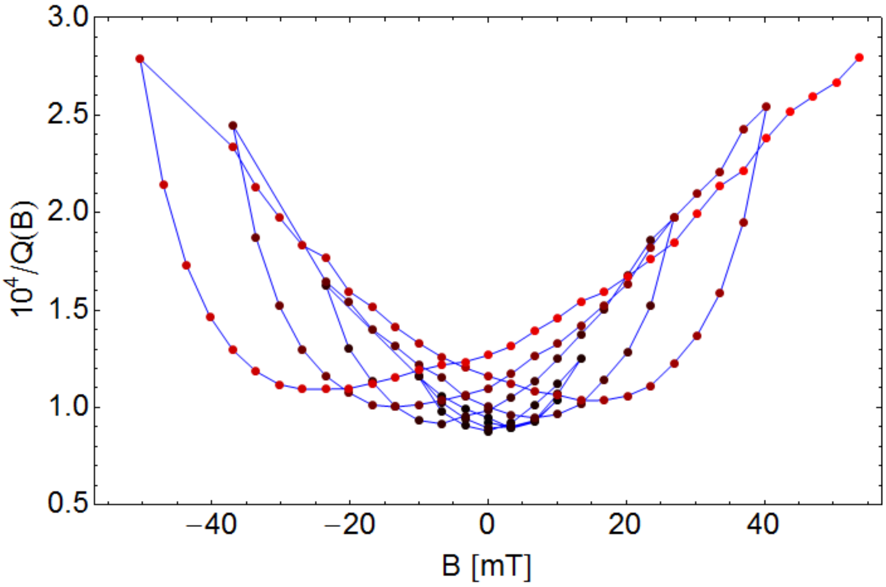

Figure 36: The inverse of the quality factor of the resonator due to an alternating rise in the magnetic field. Only the first few maximal values of Figure 35b are displayed.

one can observe the transition of the curve shape. One can compare these curves also with Figure 31. For low fields, the curve looks rather parabolic. It resembles the shape of the curve of a resonator that has holes in the center conductor. But from some field strength on, the shape changes to look like the one observed in the hysteresis measurement with fields of some 50 mT for resonators with no holes. This gives the impression, that there is a change in the underlying physics as the magnetic field reaches a certain value. And this value seems to be higher if there are holes in the resonator.

Following the hand-waving argument given above, this could mean that there are some pinning centers in the center conductor of the resonator, but they are not strong. Therefore, a lower field is needed to see the same effect as before in the case of a threaded center conductor. This hypothesis could be tested by investigating at which value the shape of the curve of a threaded resonator changes.

7 Hysteresis Measurement in the Arctic

There have been several problems with the coils in the Arctic so far. The first is a mistake during the calculation of the field strength that lead to an overestimation of the actual field by a factor of three. Then, because

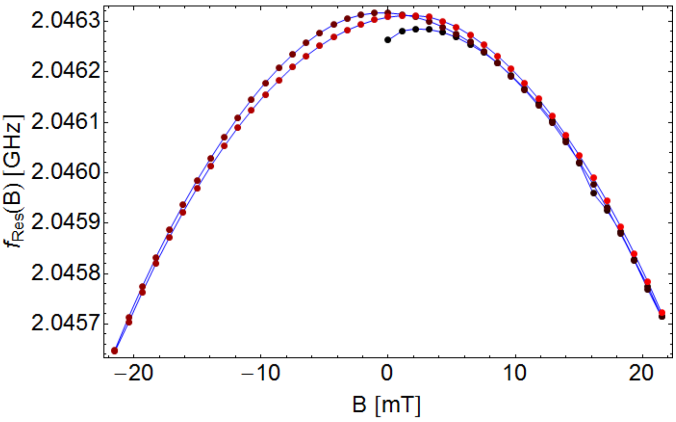

(a) The behavior of the resonance frequency upon an alternating rise of the magnetic field.

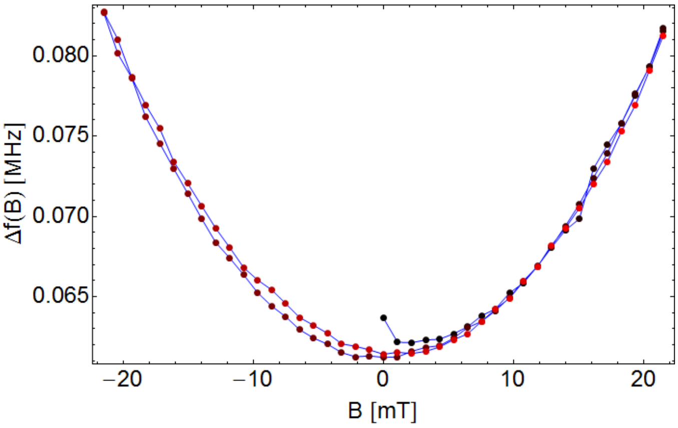

(b) The peak width upon an alternating rise of the magnetic field.

Figure 37: The magnetic field, plotted in mT, is raised in an alternating way. The plotted curves are the resonance frequency and the peak width. The measurement was performed in the Arctic.

the thermalization of the coils is not as optimal as when they are dipped in liquid helium, quenches occur already at currents of some 60 mA. Therefore, Hysteresis curves could only be taken with fields up to 22 mT. The sample used is again a resonator with holes in the center conductor. In Figure 37, the resonance frequency and the peak width of this hysteresis curve are plotted. Note that the axes are still given in the same units as for the plots that show measurements done with the dipstick. The resonance frequency is some 10 MHz higher, and the peak width is almost an order of magnitude lower than before. This leads to a higher quality factor and lower losses, as

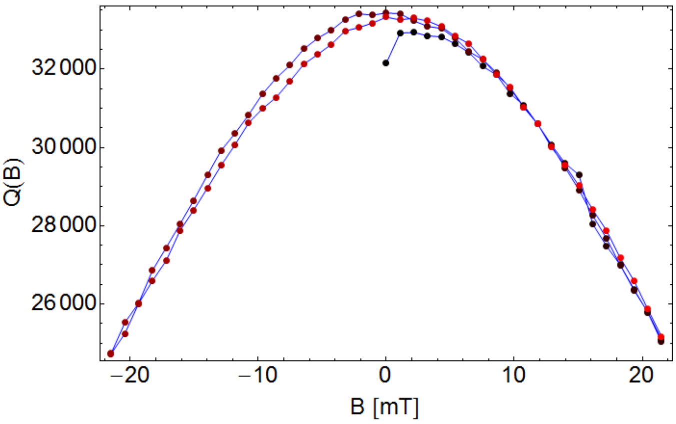

(a) The behavior of the quality factor upon an alternating rise of the magnetic field.

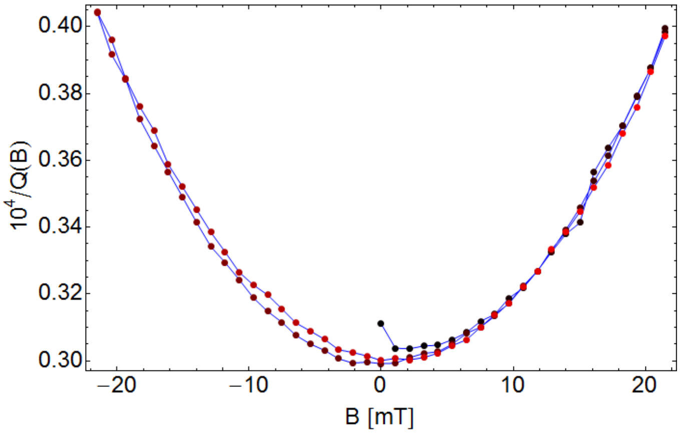

(b) The total losses times 10^4 upon an alternating rise of the magnetic field.

Figure 38: The magnetic field, plotted in mT, is raised in an alternating way. The curves shown indicate the quality factor and the total losses of the resonator. The measurement was performed in the Arctic with a sample that has holes in the center conductor of the resonator.

shown in Figure 38.

The feature that strikes the viewer first is again the parabolic shape of the curve, as already discussed in Sections 6.2 and 6.3. Also there is almost no hysteresis. The latter has two possible reasons. First, the field is clearly more homogeneous in comparison to the field in the dipstick. This means, that all of the resonator feels approximately the same field. This is not the case in the measurements using the dipstick. Second, the temperature this curve was obtained at is some 3.2 K. This temperature difference to the

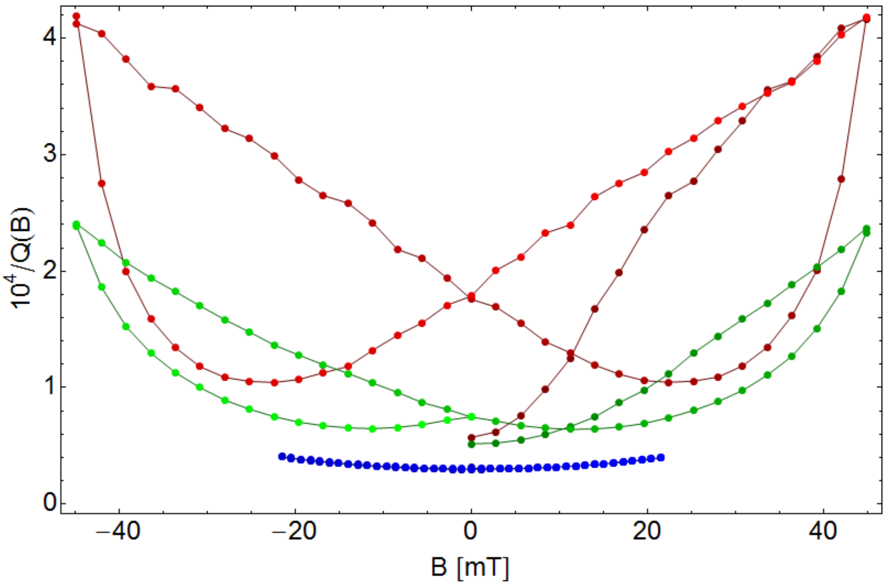

Figure 39: This Plot shows the data from Figures 27b, 30b and 38b. The red curve is a resonator without holes at 4.2 K, the green curve is a resonator with holes at 4.2 K and the blue curve is a resonator with holes at 3.1 K.

dipstick measurements has a big influence on the superconducting properties of the resonator. One can think about this in a way that the share of superconducting electrons is still changing rapidly with temperature.

The origin of the parabolic shape is not yet clear. This curve could not be fitted in a meaningful way with the models discussed beforehand. It seems that this regime is not accounted for in the model. One can also observe this phenomenon in the virgin up-sweeps of the measurements made with the dipstick. The very first data points do not coincide with the theoretical values predicted by the models. Clearly, the relevant physics here is not captured by the models used.

The parabolic shape of the hysteresis curve could have something to do with quasi particle excitations in the superconductor. These cold show a quadratic increase in the applied field. Another possibility is that the transport current distribution in the resonator is changed in a linear way due to the external field. This would then, with Equation 30, have a quadratic effect on the losses. But it is not clear why this should happen.

We can compare the data from Figure 38b with the data shown in Figure 31 where we compare the resonators with and without holes. This is shown in Figure 39. The red and green curves are as before in Figure 31, the blue curve shows the data from Figure 38b. Here it is apparent that the losses in the curve obtained in the Arctic are considerably lower than the ones in the dipstick measurements. It is a factor of around 2 if the down-sweep curves are considered at 20 mT.

We can check whether the behavior of the curves is the same for fields up to a certain value. For this purpose, we can multiply the blue curve by a factor and compensated the offset. This is shown in Figure 40. We can see that the behavior of the resonator with holes is the reproduced. For the resonators without holes, the curves are matching well up to a field of 15 mT. Then, the curve for the resonator without holes starts to deviate from the parabolic behavior.

This analysis indicates that the relevant physics at low fields for these resonators is the same. However, temperature and holes have an influence on the magnitude of the losses due to the field, and also on the field strength for which the behavior of the resonator changes. But the parabolic shape of the curves is still not explained, and needs further investigation.

8 Angle Dependence of the Quality Factor

As a final measurement series, the angle dependence of the quality factor is presented. For this, the designed sample holder has been used. The sample is a resonator with holes in the center conductor.

These measurements are somewhat laborious to make. This is because the slow parameter, the angle, can not be varied directly from Cleansweep, the program that performs the measurement. This means that each angle has to be set by hand, and therefore a measurement series requires a lot of attendance time of the experimentalist. This is also why the following plots have a relatively low resolution. Also, the plots will have a relatively big spread in the data. In order to rule out several possible sources of noise, there are some characterizing measurements presented.

To get an estimate of the standard deviation of the quality factor, a transmission spectrum was repeatedly measured. This has been done both at zero field, see Figure 41a, and at a field of ≈17 mT, as shown in Figure 41b.The standard deviation in the quality factor is about 150. There seem to be some tendencies, especially when the measurement is repeated for a sourced field.

In order to rule out a possible effect of the heating due to mechanical motion, an angle dependent series of transmission spectra was recorded, as shown in Figure 42. The angle is given by the number of steps the stepper motor performed. Each step would turn the micro meter screw by 0.9° and therefore tilt the coils. Zero steps correspond to the situation at room tem-

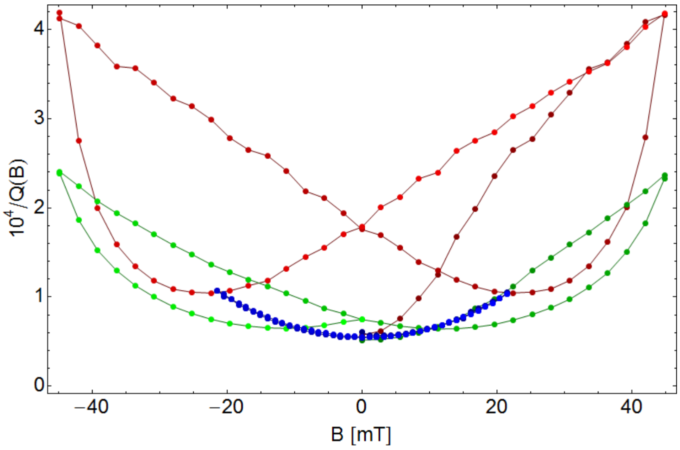

(a) The blue curve is multiplied with a factor of 5 and compensated for the offset to fit the green curve.

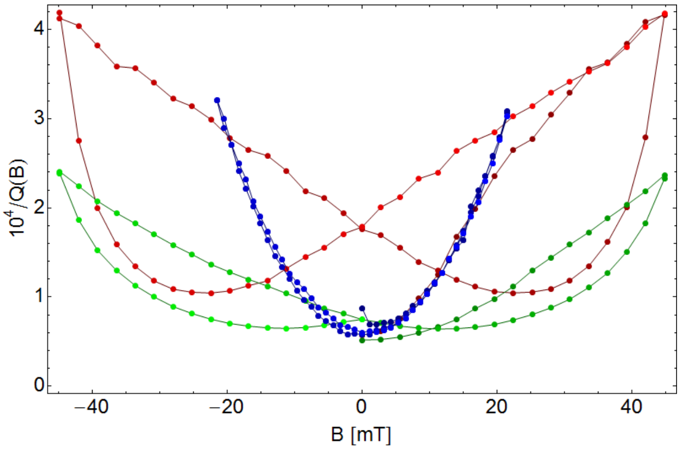

(b) The blue curve is multiplied with a factor of 25 and compensated for the offset to fit the red curve.

Figure 40: The data from Figure 39 is displayed. The red curve indicates the losses in a resonator without holes, the green curve shows the losses in a resonator with holes. The blue curve shows the losses of a resonator with holes, measured in the Arctic, multiplied with a factor.

perature where the micrometer screw just touches the plate protecting the coils, compare Figure 7. At 400 steps, the coils are tilted by an angle of 1.6°. It seems that here is a hysteresis in the quality factor upon the change of the angle of the coils. But it needs to be mentioned that this is still within the standard deviation.

As we source a field and perform the angle dependent measurement, we

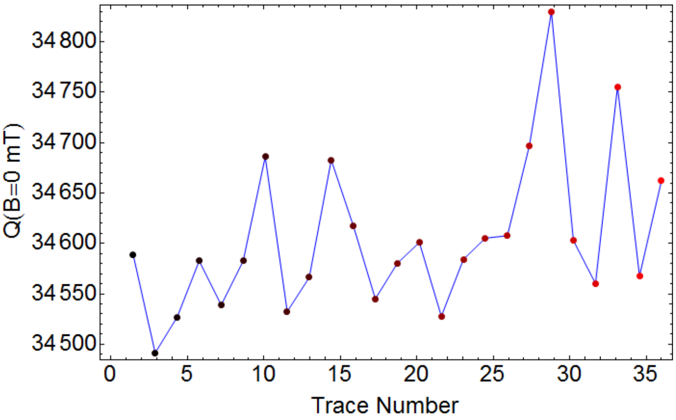

(a) Repeated measurements of the quality factor at zero applied field.

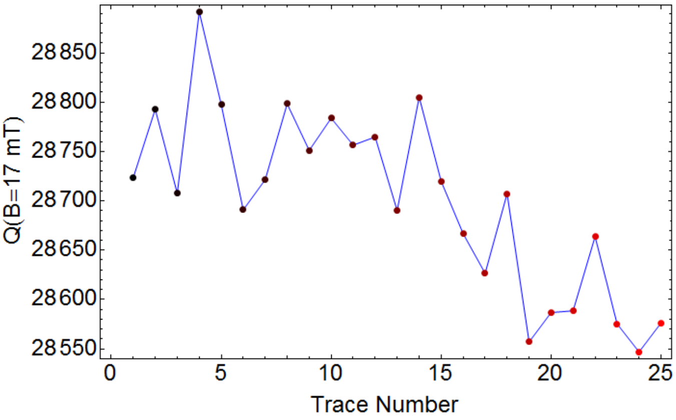

(b) Repeated measurements of the quality factor at a field of ≈17 mT.

Figure 41: To get an idea of the standard deviation in the quality factor, the transmission spectrum was measured repeatedly. The obtained quality factor is plotted for the subsequent repetitions of the measurement.

can see a change in the quality factor and in the losses of the resonator, as shown in Figure 43. In that measurement, a field of 22 mT was sourced. The angle sweep started at 200 steps, went twice up to 400 and to zero, and ended at 200 again. Like this, a better comparability can be achieved. We can see that the change in the quality factor and the losses is substantial. The losses due to the change in the angle are roughly half of the losses due to the magnetic field, as we have seen in section 7.

However, it is interesting to note that there is no clear maximum in the quality factor for an angle other than 0. This might be due to the fact that

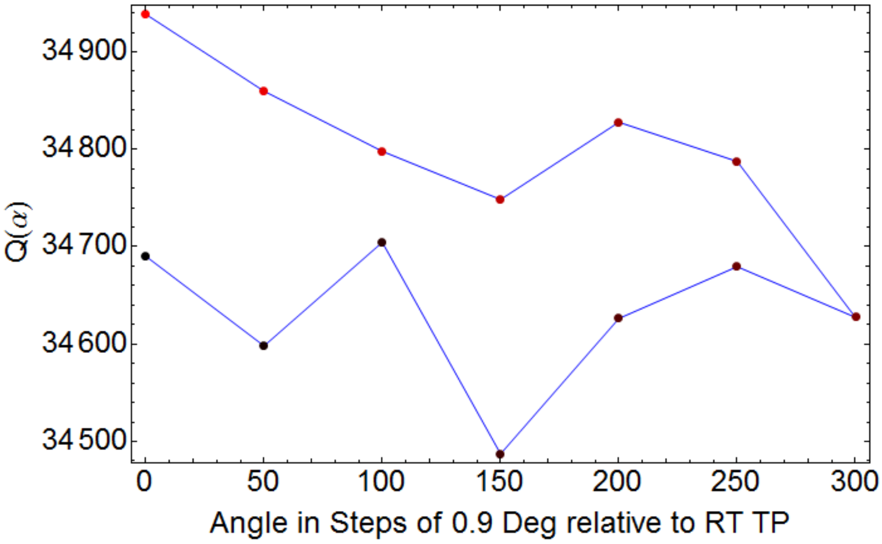

Figure 42: The quality factor of the resonator when the coils are being tilted. The tilting is measured in number of steps of 0.9° of the micrometer screw relative to the Room Temperature Touching Point. No field is sourced.

the coils are already tilted too much, meaning that turning the micrometer screw can just increase the angle, and not decrease it.

Out of this reason, the measurement was repeated, and the equilibrium position of the coils was set to an extreme, such that the angle can be varied as much as possible. The result of this measurement is shown in Figure 44. As the angle is increased, an increase in the quality factor can be observed. This indicates, that the coils are being tilted in the right direction if we try to minimize the losses. Then, at 1300 steps, the quality factor reaches a maximal value. Further increase of the angle only lowers the quality factor. As the angle is then decreased again from its maximal value, there seems to be a mechanical hysteresis. This means that the beryllium copper tubes of the flexure bearing slipped in their copper mounting. This is why the quality factor is then relatively independent of the angle of the micro meter screw. The screw does not press against the coils any more, they just have a new equilibrium position.

It has to be noted that after opening the fridge, one could observe that the coils were not in the same equilibrium position any more. However, the position of the coils is not on an extreme angle, but relatively close to the an angle of 0°. This indicates that the assumtion of a mechanical hysteresis is justified, although the measurement data in Figure 44 suggests that the

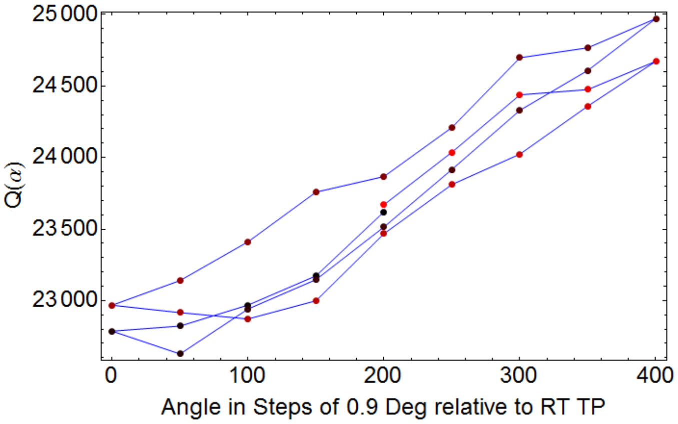

(a) The quality factor of the resonator as the angle of the coils is changed.

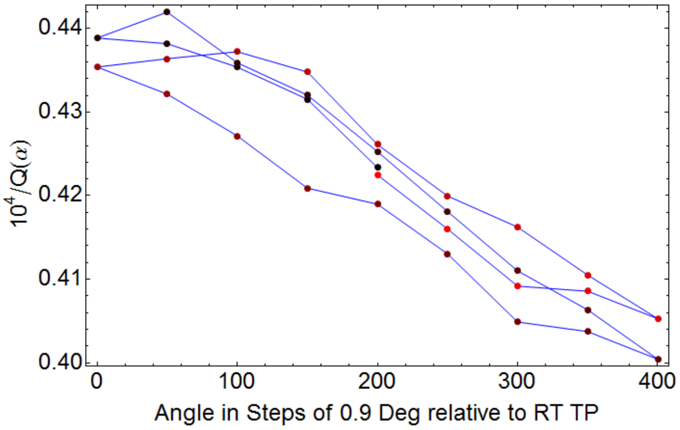

(b) Total losses in the resonator as the angle of the coils is changed.

Figure 43: The angle of the coils is changed for a field strength of 22 mT. The starting point of the experiment is at 200 steps, and so is the end point. For better comparability, two angle sweeps are performed.

angle of the coils should be closer to an extreme value because the quality factor did not change any more. This could be a wrong assumption, as the quality factor on the other side of the maximum also has a relatively flat behavior. A repetition of the measurement that would go to higher angles could be performed to gain certainty about the hysteretic behavior of the losses in the angle dependence. So far it was not performed because of the danger of breaking the coils.

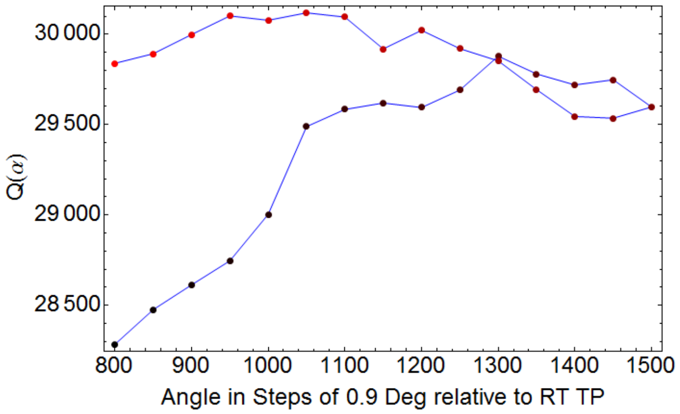

(a) The quality factor of the resonator as the angle of the coils is changed.

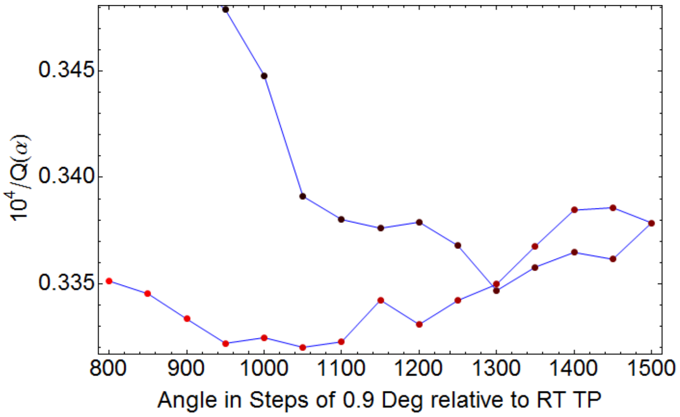

(b) Total losses in the resonator as the angle of the coils is changed.

Figure 44: The angle of the coils is changed for a field strength of 17 mT. Note that the x-axis is not with respect to the same reference point as Figure 43. Towards the end of the angle up-sweep, a maximum in the quality factor, respectively a minimum in the losses can be seen.

This measurement means that indeed the angular dependence of the field is important. But this statement has to be taken with care, as in a certain angle range, the quality factor does only increase by some 5 %. As the effort to build a mechanical access into a fridge is high, it is probably not worth having tiltable coils in a next generation of such a sample holder. The data in Figure 44 is not very nice, it has a lot of noise, a rather low resolution and shows a mechanical hysteresis. Still, it captures the feature we wanted to measure, namely that there is a minimum in the losses for a certain angle between field and sample.

9 Summary and Conclusion

In the beginning of this thesis we built a sample holder with tiltable coils. We used it to measure the losses in coplanar waveguide resonators due to the viscous motion of Abrikosov vortices. We developed an analytical expression for this dissipation and approximated data obtained from the experiments with the model.

The design of the sample holder followed the requirements of the measurement. The most important feature is that the coils source a homogeneous field which is tiltable. The latter was realized using flexure bearings.

The theory part of this thesis started with a brief introduction to Type-II superconductivity. Based on the assumption of a viscous motion of vortices, a model describing the dissipated power due to the vortex motion was derived. We have seen that this description requires models of the current and the magnetic field in the resonator. It was argued that only current models describing a current density due to a transport current in the resonator are feasible. Also, only models for the field in the resonator that result from an externally applied field lead to dissipation that is detectable with the setup used. Crude estimations of the parameters used in the models were given.

Measurements were taken in two surroundings. First, a liquid helium dewar and a dipstick were used to confirm that holes in the center conductor of a superconducting coplanar waveguide resonator reduce the dissipation due to applied magnetic fields. Second, a dry fridge and the designed sample holder enabled measurements at low fields with an angular dependency.

There is a considerable amount of literature studying the behavior of resonators in perpendicular magnetic fields, for example Refs. [19,39,40]. But so far, there are only a few papers describing the behavior of resonators in parallel magnetic fields [20]. New in the presented setup is an adjustable angle between the magnetic field and the sample. Also, a quantitative description of the behavior of the resonators from a certain field strength on is given. Other authors (again Ref. [20]) did not think this to be possible.

In this thesis, it was shown that the hysteretic behavior of losses in resonators can be reduced if the center conductor of the resonators is threaded by holes. Also, the absolute losses due to magnetic fields are lowered if there are holes in the center conductor.

There seem to be two different regimes during the up-sweep of the magnetic field from the virgin state. In the beginning, the losses increase quadratically. This behavior is not yet understood. But from a certain field on, the losses follow a different law. At these higher fields, the behavior of the losses can be described by the model developed in this thesis. The field at which the transition between the two different models occurs seems to depend on temperature and presence of holes in the center conductor of the resonator.

The losses in the resonator show an angle dependence in the applied magnetic field. It seems that there is an optimal angle of the coils with respect to the sample to reduce losses. The reduction in the losses seem to be small if the angle is close to zero. If it can be ensured that in a potential next generation of a sample holder the angle between field and sample is close to zero, the requirement of tiltable coils can be omitted.

10 Outlook

We made progress in the understanding of the behavior of superconducting coplanar waveguide resonators in strong parallel magnetic fields. A short time goal is to get an understanding of the behavior of the resonator at low fields. This could be achieved by the explicit incorporation of the parallel component of the magnetic field to the model. Also, it is important to find an expression for the field strength where the transition between the quadratic and the hysteretic loss regimes occurs.

A further step will be to place some organic molecules on the resonator. This should enable us - in an NMR-like way - to observe a coupling between the spins and the resonator. This would serve as a proof of principal measurement for the idea of a Nano-NMR. If we can not observe a coupling, probably a next generation of sample holder and coils will be built. In this generation one could think of leaving away the tiltability of the coils.

A nice application would be to put the sample in a gradient field. The spin splitting of the electrons is then position dependent, and a space resolved imaging would be possible.

Depending on how well the frequency of the spin splitting can be determined, it could also be possible to determine the surrounding of an electron. As the surrounding (like neighboring nuclei) influences the local magnetic field the electron feels, it could in principle be possible to draw conclusions about the structure of a molecule.

For these applications it would be favorable to go to lower temperatures. The energy $E = \boldsymbol{\mu}_0 \cdot \boldsymbol{B}_0$ for an electron in a magnetic field of $0.3\,\mathrm{T}$ is $2.8 \cdot 10^{-24}\,\mathrm{J}$, whereas the thermal energy $k_B T$ at $3\,\mathrm{K}$ is given as $4.1 \cdot 10^{-23}\mathrm{J}$. Assuming a thermal equilibrium, the probability of finding a spin in the excited state - anti-parallel to the applied field $\boldsymbol{B}_0$ - is proportional to the Boltzmann-factor $\exp(E/k_BT)$. The probability to find it in the ground state is proportional to $\exp(-E/k_BT)$. Assuming these are the only occupied levels, we we get that $\approx 47\,\%$ of the spins is in the excited state. This could be improved if the temperature was lowered to 1.5 K. Then, approximately 43 % of the spins would be in the excited state. This would yield a better signal. Also, the noise level would decrease, resulting in a better detection.

It would also be interesting to try reducing the losses due to vortices further by using the 'ratchet effect' [41]. This effect uses a saw-tooth function like modulated vortex pinning potential of the superconducting strip to drive vortices out of the strip upon application of a transport.

Another application is that one could think of such spins as qubits. As the spins have a very long lifetime, they would be useful to serve as a "quantum hard drive" in a quantum computer architecture [42, 43]. The processing of the quantum computer would be performed in superconducting qubits which have low gate times. If a state is not needed for a moment, it could then be parked in a spin qubit, where it would be less prone to decay.

11 Acknowledgment

First of all, I want to thank Prof. Dr. Andreas Wallraff for giving me the opportunity to work in the Quantum Device Lab here at ETH Zürich. This was a great opportunity for me to learn a lot, about physics, academia, engineering and science in general. Then, I would also like to thank my supervisor Dr. Milan Allan for providing such an interesting and diverse project. Also, I am grateful that he gave me a lot of freedom to work on most of the tasks. I really learned to appreciate that I had time to think on my own about a variety of problems and challenges that arose during my thesis. It is incomparably more satisfying to get stuck and remedy the obstacle on your own than watching someone do that for you.

Also, I would like to thank Janis Lütolf who has indefatigably provided me with advice to hundreds of design and engineering questions, although he would probably say the number was rather in the thousands. He was a great support, and facilitated my life in the workshop greatly. I would also like to mention Yannick Hmina who also helped me on a regular basis in the workshop and built the bearing of the stepper motor. The FPGA used in this setup was programmed by Yves Salathé who put a lot of work into it. Moreover, he provided very competent IT support, for which I am grateful.

Many thanks go to the whole D7 office for many good laughs and nice company. I especially want to mention Johannes Heinsoo who knows every trick in the book when it comes to Mathematica. I really enjoyed our late-night and weekend physics sessions.

The nice atmosphere in the group will stick to my memory. Be it an intense strategy meeting, an exhausting ordinary work day or a well-earned, malt based, refreshing drink in the evening, it is fun to be part of such a motivated team.

References

[1] Frank Pobell. Matter and Methods at Low Temperatures, Third Edition. Springer.

[2] Vacuumschmelze GmbH & Co. KG, Cryoperm 10. http://www.vacuumschmelze.com/index.php?id=1058

[3] MuShield Company, Cryoperm. http://www.cryopermshielding.com/cryoperm-shielding.html

[4] G. Puebla-Hellmann. DC, Microwave and Optical Measurement Schemes for Nano-Scale Devices. PhD thesis, ETH Zürich (2012).

[5] Supercon Inc., Fine SC Wires. http://www.supercon-wire.com/content/fine-sc-wires

[6] Nukephysics.com, Finite Length Solenoid Potential and Field. http://nukephysik101.files.wordpress.com/2011/07/finite-length-solenoid-potential-and-field.pdf

[7] E. E. Callaghan and S. H. Maslen. The Magnetic Field of a Finite Solenoid. NASA, Technical Note D-465.

[8] Rainer Zoufal, About writing a Master thesis

[9] Schweizer-FN. Update 07.11.2013. www.schweizer-fn.de

[10] Wikipedia, Torsion. Update 24.05.2014. http://de.wikipedia.org/wiki/Torsion_(Mechanik)

[11] J. M. Kosterlitz, D. J. Thouless. J. Phys. C: Solid State Phys. 6 1181.

[12] Michael Tinkham, Introduction to Superconductivity, Second Edition. Dover Publications, Inc.

[13] C. P. Poole Jr., H. A. Farach and R. J. Creswick. Superconductivity. Academic Press, 1995.

[14] W. Meissner and R. Ochsenfeld. Naturwissenschaften 21, 787 (1933).

[15] F. London and H. London. Proc. Roy. Soc. (London) A149, 71 (1935).

[16] A. B. Pippard. Proc. Roy. Soc. (London) A216, 547 (1953).

[17] j. Bardeen, L. N. Cooper, and J. R. Schrieffer, Phys. Rev. 108, 1175 (1957).

[18] J. Bardeen and M. J. Stephen. Phys. Rev. 140, A1197 (1965).

[19] C. Song, T. W. Heitmann, M. P. DeFeo, K. Yu, R. McDermott, M. Neeley, J. M. Martinis, B. L. T. Plourde. Phys. Rev. B 79, 174512 (2009).

[20] D. Bothner, T. Gaber, M. Kemmler, D. Koelle, R. Kleiner, S. Wünsch, M. Siegel. Magnetic hysteresis effects in superconducting coplanar microwave resonators. Phys. Rev. B 86, 014517 (2012).

[21] D. E. Oates, S.-H. Park, G. Koren. Phys. Rev. Lett. 93, 197001 (2004).

[22] David M. Pozar. Microwave Engineering. Second Edition. John Wiley & Sons, Inc (1998).

[23] M. V. Göppl. Engineering Quantum Electronic Chips - Realization and Characterization of Circuit Quantum Electrodynamics Systems. PhD thesis, ETH Zürich (2009).

[24] R. P. Huebener, R. T. Kampwirth, R. L. Martin, T. W. Barbee Jr., R. B. Zubeck. IEEE Transactions on Magnetics, vol. MAG-11, No.2, March 1975.

[25] A. A. Abdumalikov Jr.,V. V. Kurin, C. Helm, A. De Col, Y. Koval and A. V. Ustinov. Nonlocal electrodynamics of long ultranarrow Josephson junctions: Experiment and theory. Rhys. Rev. B 74, 134515 (2006).

[26] Gabriel Puebla-Hellmann. Personal correspondence.

[27] Peter Lahl, Roger Wördenweber. Appl. Phys. Lett. 81, 505 (2002).

[28] K. H. Bennemann, J. B. Ketterson. Superconductivity, Conventional and Unconventional Superconductors, Volume 1. Springer, 2008.

[29] W. T. Norris. Calculation of Hysteresis Losses in Hard SUperconductors Carrying AC: Isolated Conductors and Edges of Thin Sheets (1969).

[30] E. H. Brandt, M. Indenbom. Type-II-Superconductor Strip with Current in a Perpendicular Magnetic Field. Phys. Rev. B, Volume 48, Number 17 (1993).

[31] C. P. Bean, Magnetization of High-Field Superconductors. Review of Modern Physics, 1964.

[32] C. P. Bean, Magnetization of Hard Superconductors. Phys. Rev. Lett, Volume 8, Number 6, 1962.

[33] D. Walls & G. Milburn. Quantum Optics. Springer-Verlag, Berlin (1994).

[34] R. A. Bianchetti. Control and Readout of a Superconducting Artificial Atom. PhD thesis, ETH Zürich (2010).

[35] J. M. Fink. Quantum Nonlinearities in Strong Coupling Circuit QED. PhD thesis, ETH Zürich (2010).

[36] D. Bothner, T. Gaber, M. Kemmler, D. Koelle and R. Kleiner. Improving the performance of superconducting microwave resonators in magnetic fields. Appl. Phys. Lett. 98, 102504 (2011).

[37] C. Song, M. P. DeFoe, K. Yu and B. L. T. Plourde. Reducing microwave losses in superconducting resonators due to trapped vortices. Appl. Phys. Lett. 95, 232501 (2009).

[38] D. Bothner, C. Clauss, E. Koroknay, M. Kemmler, T. Gaber, M. Jetter, M. Scheffler, P. Michler, M. Dressel, D. Koelle and R. Kleiner. Reducing vortex losses in superconducting microwave resonators with microsphere patterned antidot arrays. Appl. Phys. Lett. 100, 012601 (2012).

[39] S. Guénon, Y. J. Rosen, A. C. Basaran, I. K. Schuller. Highly effective superconducting vortex pinning in conformal crystals. Appl. Phys. Lett. 102, 252602 (2013).

[40] G. Stan, S. B. Field and J. M. Martinis. Critical Field for Complete Vortex Expulsion from Narrow Superconducting Strips. Phys. Rev. Lett. 92, 097003 (2004).

[41] C.-S. Lee, B. Jankó, I. Derényi and A.-L. Barabási. Reducing vortex density in superconductors using the 'ratchet effect'. Nature 400, 337-340 (1999).

[42] A. Imamoglu. Phys. Rev. Lett. 102, 083602 (2009).

[43] C. Monroe, R. Raussendorf, A. Ruthven, K. R. Brown, P. Maunz, L.-M. Duan and J. Kim. Large-scale modular quantum-computer architecture with atomic memory and photonic interconnects. Phys. Rev. A 89, 022317 (2014).

[44] CMR direct, Stycast 1266.
http://www.cmr-direct.com/de/cmr-epoxy-1266-1kg

Appendix

A Stycast 1266 Recipe

Here, we briefly present how to make a Stycast 1266 cylinder. It is important to be aware of the fact that the surface of the cylinder will not be very nice and workshop will need to cut away a substantial layer from it. Therefore it is advisable to make the diameter of the cylinder at least one centimeter bigger than necessary. Also, the length should be at least 3 centimeters more than required, as it needs to be fixed somehow in the lathe.

To make such a cylinder, we need:

- Enough Stycast 1266, Part A and B
- A metal disk serving as the bottom of the casting mold
- A hollow metal cylinder serving as the walls of the casting mold
- Teflon foil serving as backing of the casting mold
- A metal bar and screw clamps to press together the bottom disk and the hollow cylinder
- A vacuum flask
- An *old* vacuum pump which may get contaminated
- A lot of aluminum foil to cover the work space

The casting mold to pour the Stycast into should be prepared beforehand. It turned out to be helpful to use a metal disk as bottom and a hollow metal cylinder as walls. All the faces touching Stycast later on should be covered with Teflon foil to prevent sticking. Then, put a metal bar on top of the hollow cylinder and fix it tightly with small screw clamps such that there is a uniform pressure of the hollow cylinder on the disk. Check now, whether or not the casting mold with the screw clamps fits into the vacuum flask.

Note that it is not a good idea to use plastic (especially PET) or glass to make the casting mold. The former will react with the Stycast, leading to a degraded quality of the product, see Figure 45a. The latter will make it fairly difficult to get the Stycast out of. Also, do not use Teflon Spray instead of Teflon foil, in our case this also degraded the quality of the product (it turned dark and was rather brittle).

Then, cover the whole workspace generously in aluminum foil (including the vacuum flask), as this process has a high mess-potential. Mix the Stycast

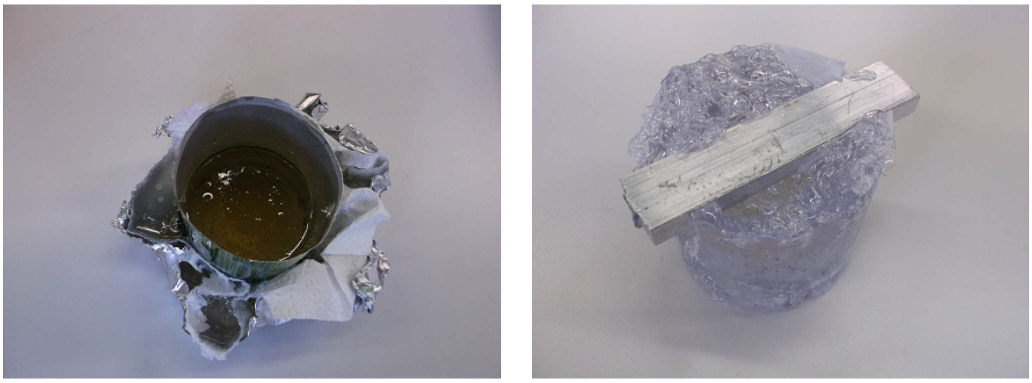

(a) Stycast apparently reacts with Teflon spray. The color changes and the mechanical properties are not as good anymore.

(b) The Stycast started boiling during the hardening. Due to a lack of success in removal attempts, the metal bar used to press the metal cylinder on the bottom is shown as well.

Figure 45: Different stages in the improvement process for the Stycast recipe.

in a separate container. The mixture ratio is 28 weight parts of component B for all 100 weight parts of component A, [44]. Stir it well, and pour it after some 20 minutes of stirring into the casting mold. Then, put it into the vacuum flask and turn on the pump. The pressure we used was ≈ 0.1 bar. Wait until the bubbles start rising to the surface. This takes a couple of minutes, and they should stop raising some ten minutes afterwards. Then, carefully release the vacuum and let the Stycast harden for 24 hours. Now, the Stycast can be taken out of the mold. If it sticks in spite of the Teflon foil, the usage of a rubber hammer may be helpful. Only the surface of the Stycast cylinder gets affected by this procedure.

Note that it is important to release the vacuum. The hardening is an exothermal process, and if the pressure of the surrounding is low the boiling point is low. This will then lead to the boiling of the Stycast, resulting in something as shown in Figure 45b. Also, the vacuum enhances the quality of Stycast as it has less air bubbles enclosed afterwards.

The final result is shown in Figure 46. It is transparent, and there are no enclosed bubbles in the center of the block.

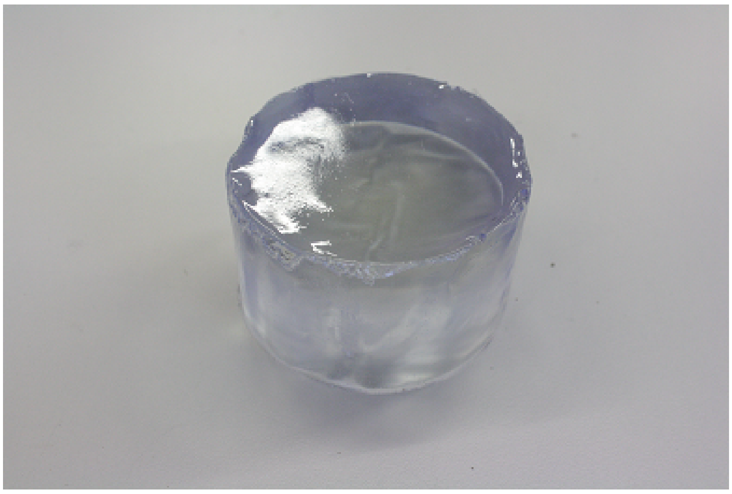

Figure 46: The final result is a transparent Stycast cylinder with almost no enclosed air bubbles.

B Physical Properties of the Niobium CPW Resonators

Experience shows that it can be both hard and annoying to find simple physical parameters and material properties needed. Therefore, we present here a table that briefly summarizes the physical properties of the niobium resonators we used. Listed are different parameters and their values, the symbol used for them in this thesis, and where possible a source for the value is stated.

Parameter	Symbol	Value	Source
Material		Niobium	
London penetration depth	λ_L	32-100 nm	Refs. [13,25]
Critical temperature	T_C	8.67 K	Ref. [23]
Resistivity above T_C	ρ_C	$5.8 \cdot 10^{-8}\,\Omega\text{m}$	Ref. [23]
Upper critical field	B_{C_2}	1.98 T	Ref. [13]
Critical current density	j_C	$2 \cdot 10^{10}\,\text{A/m}^2$	Sec. 4.4
Thickness	d	150 nm	Design
Center conductor width	S	$9.5\,\mu\text{m}$	Design
Gap size	W	$5\,\mu\text{m}$	Design
Resonator length	l	32 mm	Design
Line inductance	L'	390 nH/m	Eqs. 40, 41
Resonance frequency	f_{Res}	2 GHz	Measurement
Effective permeability	ε	5.5	$\nu\lambda = c/\sqrt{\varepsilon}$
External losses	κ	0.1 MHz	Measurement
Internal losses	γ	0.1 MHz	Measurement
Hole diameter	ϕ	$0.8\,\mu\text{m}$	Design
Hole spacing	δ	$1.2\,\mu\text{m}$	Design

Note that the parameters λ_L T_C, ρ_C and j_C are geometry dependent and differ from the bulk values. Also, the value for B_{C_2} is a bulk value and it is unclear what the actual critical field for a thin strip is.

For the internal and external losses the definition

$$Q = \frac{f_{Res}}{2\kappa + \gamma}$$

is used. The internal losses are to be understood without field induced losses.

C File Locations

In order to facilitate the reproducibility of simulations and data analysis we will list in this section where data, simulations and designs are saved. In order to get access to them, the network drive Q used in the Quantum Device Lab needs to be mounted, see the groups Wiki-Page. The location of the files is then given relative to the folder *Q:\USERS\Florian\Masterthesis*.

C.1 Designs

For the design of the sample holder the program Autodesk Inventor Professional 2014 - Educational Institution Version is used. The parts and assemblies are strored in the folder *Inventor_Designs*. The final design of the sample holder is *Inventor_Designs\Sample_Holder* and is called *Horizontal_Assembly.iam*. From this, all the parts can be accessed.

C.2 Data Sheets

The information to the devices used can be found in the folder *References\Datasheets*. For example the mechanical parts, stepper motor, couplings and rotary feed through as well as the information to the current source can be found there.

C.3 Simulations

The estimation of the current in the resonator, section 4.3 is made in the Mathematica file in *Mathematica_Files\PowerInResoantor*. The calculations for the kinetic inductance change in section 6.2 are made in the *Mathematica_Files\KineticInductance* folder.

The models used to fit the data are in files that are in the folder *Mathematica_Files\FittingData*. The files should be identifiable by its names. In the files that are named starting with *DefinitionsFast*, the models used are saved. There, the models are evaluated only at a number of data points, not continuously. The files ending on *FitFinder* are written to find a fit to the data that minimizes error squares. However, they take several days to be evaluated, and for the fit finding procedure the method "NMinimize" should be used such that not only a local minimum is found.

The files that generate the plots used in section 4 to visualize theoretical models can be found in *Mathematica_Files\PlotMakingFiles*.

C.4 Data

The folder *Data_Analysis* is organized in such a way that all the data obtained from measurements is stored in folders that start with the date of the cool down. The second part of the folder name indicates the sample, or whether it was measured in the dipstick. The Mathematica files used to analyze the data are stored in the folders called *Template*. In order to evaluate the file, the files with the data, the frequency list and the containing the values of the slow parameter need to be stored in the same location, and the data path needs to be indicated in the head line of the evaluating Mathematica file. The location of the data used to make plots in this thesis is summarized in the following table.

Data shown in Figure	Stored in folder *Q:\USERS\Florian\Masterthesis\Data_Analysis*
25 26 27 28 29	*20140522_Dipstick\20140525_Hysteresis80mAPort23*
30	*20140522_Dipstick\20140524_Hysteresis80mA*
32 33 34	*20140427_Dipstick*
35 36	*20140512_Dipstick\20140514_Alternating_Raise*
37 38	*20140530_Resonator_Only\20140604_50mAHyst*
41a	*20140530_Resonator_Only\20140601_Repeats*
41b	*20140530_Resonator_Only\20140601_40mA_Repeats*
42	*20140530_Resonator_Only\20140601_ZeroFieldFast*
43	*20140530_Resonator_Only\20140604_50mAAngleNew*
44	*20140607_Resonator_Only\20140611_AngleFrom800*

The VNA data for the cables is stored in the folder *VNA Data*, and there again ordered by date. The data for the cables that are currently used in the fridge, the *Q:\Arctic* folder should be checked.

ETH
Eidgenössische Technische Hochschule Zürich
Swiss Federal Institute of Technology Zurich

Declaration of originality

The signed declaration of originality is a component of every semester paper, Bachelor's thesis, Master's thesis and any other degree paper undertaken during the course of studies, including the respective electronic versions.

Lecturers may also require a declaration of originality for other written papers compiled for their courses.

I hereby confirm that I am the sole author of the written work here enclosed and that I have compiled it in my own words. Parts excepted are corrections of form and content by the supervisor.

Title of work (in block letters):

Characterization of Coplanar Waveguide Resonators in Parallel Magnetic Fields

Authored by (in block letters):
For papers written by groups the names of all authors are required.

Name(s):	**First name(s):**
Luethi	Florian

With my signature I confirm that
- I have committed none of the forms of plagiarism described in the 'Citation etiquette' information sheet.
- I have documented all methods, data and processes truthfully.
- I have not manipulated any data.
- I have mentioned all persons who were significant facilitators of the work.

I am aware that the work may be screened electronically for plagiarism.

Place, date	**Signature(s)**
Zuerich, 13.06.2014	Florian Lüthi

For papers written by groups the names of all authors are required. Their signatures collectively guarantee the entire content of the written paper.